www.sciencemag.org/content/356/6339/aai8185/suppl/DC1

# Supplementary Materials for

## Three-dimensional $Ca^{2+}$ imaging advances understanding of astrocyte biology

Erika Bindocci, Iaroslav Savtchouk, Nicolas Liaudet, Denise Becker, Giovanni Carriero, Andrea Volterra*

*Corresponding author. Email: andrea.volterra@unil.ch

Published 19 May 2017, *Science* **356**, eaai8185 (2017)
DOI: 10.1126/science.aai8185

**This PDF file includes:**



**Other supplementary material for this manuscript includes the following:**

## Materials and Methods

Antibodies and chemicals

Antibodies and chemicals Primary antibody polyclonal GFP (chicken) was from Aves Labs Inc., Oregon, USA (GFP-1010); polyclonal glutamine synthetase (rabbit) from Abcam, Cambridge, UK (ab73593); monoclonal NeuN (mouse) from Merck SA, Switzerland (MAB377); aquaporin-4 (rabbit, ab2218) and monoclonal glial fibrillary acidic protein (GFAP) antibody (mouse, ab3402) were from Millipore. Secondary antibodies Alexa Fluor 555 (rabbit), Alexa Fluor 488 (chicken and mouse) and Alexa Fluor 633 (chicken and mouse) as well as 4′,6-diamidino-2-phenylindole (DAPI) were from Thermo Fisher Scientific Inc., MA USA. 4-aminopyridine (4-AP) was from Tocris Bioscience, Bristol, UK (ref.0940); Tetrodotoxin (TTX) from Latoxan, France (ref L8503). All the other chemicals were from Sigma-Aldrich.

Transgenic mice

For astrocyte $Ca^{2+}$ imaging experiments, two transgenic mouse lines, a *lox-STOP- lox-cytosolicGCaMP6f* (purchased from The Jackson Laboratory http://www.jax.org, JAX 024105 (*B6;-Gt(ROSA)26Sortm95.1(CAG-GCaMP6f)Hze/J*), and *hGFAPCreERT2* (*44*) obtained from Prof. F. Kirchhoff, University of Saarland, Germany, were crossed in order to get inducible, astrocyte-specific, cytosolic GCaMP6f expression (*GFAPCreERT2xGCAMP6f* mice). At P21, double transgenic animals of both genders were weaned and group-housed. At a given age, which depended on the type of experiment (see below), mice were then treated with Tamoxifen, to induce Cre-loxP recombination via nuclear translocation of Cre-ERT2 and trigger GCaMP6f expression. Tamoxifen was dissolved in corn oil (10mg/ml) and administered i.p. (0.1 ml/10 g body weight) over 2-3 days. $Ca^{2+}$ imaging experiments in hippocampal slices were performed 10-14 days after the first Tamoxifen injection, when GCaMP6f expression was astrocyte-specific in the whole hippocampus, except for a small sub-population of neural stem cells/immature neurons in the dentate gyrus (for details see Fig. S1). For most of these experiments mice were used at P30-P65. Experiments in cortical slices were performed in older mice (4 months) to allow comparison with the in vivo dataset (see below); in this area of the brain GCaMP6f expression was astrocyte-specific even several weeks after Tamoxifen injections. In experiments involving axonal stimulation, mice were 2-4 months-old because of preceding AAV tracer injection procedure (see below). For *in vivo* $Ca^{2+}$ imaging experiments, Tamoxifen was injected directly after surgery (1 time and, in some cases, 1 day later again) into 2-3 months-old mice and mice were imaged from 11 days up to 8 weeks after the first injection. For morphological analysis of astrocytes, *GFAP-EGFP* mice *(45)* were used at P30-P56.

All *in vivo* and *ex vivo* procedures on the mice here described were conducted under license and according to regulations of the Cantonal Veterinary Offices of Vaud (Switzerland).

Viral constructs and injections

Adeno-associated virus expressing the red fluorescent protein, tdTomato under the control of the neuronal-specific promoter, synapsin (AVV2-Syn-pQC membrane tdTomato IX, viral titer: ~$1x10^{12}$ VG/ml; provided by Tebu-Bio GmbH, Germany) was injected in layers II-III of the entorhinal cortex (mEC) of *CL7BL6* or *GFAPCreERT2xGCaMP6f* mice in order to label their axonal projections to the molecular layer of the hippocampal dentate gyrus (DG), the perforant

path (PP). In some experiments, injections in the same location were performed with an AAV expressing the red $Ca^{2+}$ -sensitive indicator, jRCaMP1a under synapsin promoter (AAV1-Syn-NES- jRCaMP1, generously provided by L. Looger, Penn Core). To evaluate neuronal response to axonal stimulation, several mice carrying the floxed GCaMP6f gene were injected with a neuronally-targeted AAV5.CamKII:Cre virus into the Dentage Gyrus, leading to neuronal expression of the $Ca^{2+}$ indicator. Viral injections were performed under general anesthesia using continuous isoflurane (induction: 4%; maintenance: 1-2%). After inducing anesthesia, mice were injected s.c. with Carprofen (5 mg/kg), subjected to a small craniotomy and unilaterally injected with the virus by use of a stereotaxic apparatus into the left mEC (bregma: -4.5 mm; lateral: 2.85 mm; ventral: -3.30 mm). Virus injections were performed over a period of 5 to 10 min (0.5-1 µl). At the end, the needle was left in place for 10 more minutes and then gently withdrawn. Surgical wounds were sutured and mice allowed to recover on a heating pad. To minimize pain, xylocaine gel was applied on the suture and paracetamol (500 mg/250 ml) dissolved in the drinking water of the mice. Injections were performed on P30-40 mice, then allowing at least 3-4 weeks before preparing acute slices from the transfected brains, to give cells enough time to express the fluorescent protein. Tamoxifen (needed to trigger astrocyte GCaMP6f expression) was administered 10-14 days before sacrificing the animals (see above).

Immunohistochemistry

Immunostainings were performed as previously described (*46*). Briefly, *GFAPCreERT2xGCaMP6f* mice (P39, injected with Tamoxifen at P24, see above) were sacrificed with pentobarbital and transcardially perfused first with 0.9% NaCl solution and finally with 4% (w/v) paraformaldehyde in phosphate buffer (0.1 M PB, pH 7.4). Brains were then removed and stored in phosphate buffered saline (PBS, pH 7.4). 50 µm- thick horizontal slices (respectively 70 µm for aquaporin-4, AQP4, labeling) were cut on a vibratome in PBS (pH 7.4) and stored at -20° C in a solution containing ethylene glycol (30%) and glycerol (30%) in 0.05 M PB (pH 7.4) until further processing. For immunohistochemistry, slices were rinsed in PBS (3 x 10 min) and incubated for 1 h (2 h for AQP-4 staining) in 0.5% Triton-X 100 and 10% normal horse serum (NHS) in PBS to permeabilize membranes and reduce unspecific staining. Subsequently, slices were incubated with primary antibodies (anti-GFP, chicken, 1:500; anti-NeuN, mouse, 1:1000; anti-glutamine-synthetase, rabbit; anti-AQP4, rabbit; anti-GFAP, mouse, 1:1000) in 0.1% Triton-X 100 and 5 % NHS in PBS on a horizontal shaker (24 hours, 4° C). The GFP antibody was used to reveal location of GCaMP6f protein, which contains a permutated eGFP (*47*). Then, slices were washed in PBS (3x, 10 min) and incubated with secondary antibodies (goat anti-chicken Alexa 488 or 633, goat anti-rabbit Alexa 555, goat anti-mouse Alexa 633 or 488; all 1:500) overnight at 4° C in the same solution as for primary antibodies. After further rinsing (10 min) in PBS (including 1:5000 DAPI for nuclear staining) and then (2x 15 min) in PBS, slices were mounted with Fluoromount™ Aqueous Mounting Medium.

Confocal imaging

GCaMP6f expression was visualized using a Zeiss LSM 710 confocal microscope. Laser excitation wavelength was set at: 405 nm with a diode for DAPI; 488 nm and 514 nm with an Argon laser for Alexa Fluor 488 or GFP, respectively, and Alexa Fluor 555; 633 nm with a He/Ne laser for Alexa Fluor 633. Images of whole brain sections were acquired with a 10x (0.30 NA)

objective (frame average: 4, pinhole size: 1 Airy unit, resolution 1024x1024, 7x9 single images were combined to show the whole brain section). Higher zoom z-stacks were acquired with a 40x (1.30 NA) or 63x (1.2 NA) oil immersion objectives using a software and stored as .lsm files (20-40 µm, step size: 0.5-1 µm, frame average: 4, pinhole size: 1 Airy unit, resolution 1024x1024 or 512x512). To assess cell specificity of GCaMP6f expression a z-stack acquired from the three hippocampal regions, CA1, CA3, DG, was inspected in ImageJ software. Each GFP/GCaMP6f positive cell that had a clearly identified soma (DAPI staining) was checked for double-labeling with NeuN (neuronal marker) and GS (astrocyte marker) staining.

Acute brain slice preparation

For *ex vivo* $Ca^{2+}$ imaging experiments in brain slices, mice where anesthetized with isoflurane and decapitated. The brain was removed and quickly placed in ice-cold slicing solution containing (in mM): 105 sucrose, 62.5 NaCl, 2 KCl, 1.2 NaH2PO4, 25 NaHCO3, 0.5 CaCl2 and 7 MgCl2; pH was equilibrated with 5%/95% CO2/O2 gas mix. Horizontal, hemibrain slices (350 µm-thick) were cut, placed immediately in regular aCSF solution, containing (in mM) 118 NaCl, 2KCl, 2 MgCl2, 2 CaCl2, 25 NaHCO3, 1.2 NaH2PO4 and 10 glucose and used for the next 4-5 h at nearly physiological temperature (34 ˚C). In order to preclude development of epileptiform activity in slices, aCSF contained elevated $Mg^{2+}$ concentration (2 mM) and no GABA inhibitors were applied in these experiments. To visualize astrocytes during imaging experiments, we loaded hippocampal or cortical slices acutely with sulforhodamine 101 (SR101), a red dye which, under the used conditions, loads specifically astrocytes in the forebrain areas studied (*48, 49*). Dye loading was performed by placing slices in a dark chamber containing SR101 (500 nM) for 15 min, at 36 ˚C. To attenuate background signal, slices were rinsed for 15 min in aCSF before the experiments. For axonal visualization experiments, slices were loaded with SR101 at a lower concentration (50 nM) for 5 min at 34 °C.

*In vivo* awake mouse preparation

Adult *GFAPCreERT2xGCaMP6f* mice were anesthetized with isoflurane (4% during induction; 1.5-2% for maintenance in O2) and placed on a stereotaxic frame for implantation of cranial windows as previously described (*50*). Mice were injected s.c. with carprofen (5mg/kg) to reduce pain. Body temperature was maintained at 37 °C with a heating pad, eyes covered with Viscotears and skin over the skull thoroughly disinfected. An incision in the midline of the skull was done, the skull was cleaned and dried and then a circular craniotomy (diameter: 3 mm) was drilled with a high-speed drill with the center over the somatosensory cortex, approximately -1.5 anterior-posterior (AP), 2 medio-lateral (ML) mm from bregma, right hemisphere, and the bone, but not the dura, was removed. After absorbing any bleeding with absorbent sponge and rinsing the craniotomy with sterile aCSF (125 mM NaCl, 5 mM KCl, 10 mM glucose, 10 mM HEPES, 2 mM CaCl2 and 2 mM MgSO4, pH 7.4) a round coverslip (thickness #1, 3 mm diameter) was fitted into the craniotomy, sealed with Kwik-Sil and secured with bone cement mixed with cyanoacrylate glue. Then the whole skull was covered with cyanoacrylate glue and a custom-made head bar fixed over the left hemisphere with bone cement. Around the cranial window, a little pool was formed with the cement to retain water for the imaging. After surgery, mice were allowed to recover on a heating pad and paracetamol was dissolved in their drinking water for 3 days (250mg/250ml). 4-5 days after recovery, mice started to be trained to sit head fixed under the microscope for

consecutively longer time periods. $Ca^{2+}$ imaging was performed 2-4 weeks after cranial window implantation. 1-2 hours before imaging mice were injected i.v. or i.p. with SR 101 (5-10mg/ml in 0.9% (w/v) sterile NaCl solution, 20 mg/kg) as reported previously (*51*). In some control experiments, we omitted SR101 and did not notice obvious differences in the recorded astrocytic $Ca^{2+}$ activity.

Two-photon 3D $Ca^{2+}$ imaging

3D $Ca^{2+}$ imaging experiments were performed using either of two imaging setups: setup 1 was a Bruker *in vivo* Ultima IV system equipped with a 8kHz resonant galvanometer scanner and a piezoelectric actuator, coupled to a MaiTai eHP DS laser with 70fs pulse duration, tuned to 920 nm (SR101 and GCaMP6f in astrocytes) or 1020 nm (tdTomato or jRCaMP1a in axons). For dual $Ca^{2+}$ indicator experiments (simultaneous jRCaMP1a/GCaMP6f), the wavelength was set to 965 nm. Negative dispersion was optimized for each wavelength. Laser power was rapidly modulated by a Pockels cell. Imaging in brain slices and *in vivo* was performed with a 20x LUMPFL60X W/IR-2 NA 0.9 Olympus objective objective. Green (GCaMP6f) and red (SR101) fluorescences were separated by a dichroic beam splitter (t560lpxr) and passed through, respectively, an et520/40m-2p and an et610/75m-2p emission filter before being collected by GaAsP detectors. Setup 2 comprised a Bruker Ultima system equipped with an AOD scanner and a piezoelectric actuator. The light source was a Chameleon Vision II Ti:Sa laser, with 140fs pulse duration, tuned to 920 nm and negative dispersion was optimized to the used wavelength. The laser power was rapidly modulated by a Pockels cell. The set of dichroics and filters used was identical to that in setup 1, and green and red florescence were respectively collected by a GaAsP and a multi-alkali PMT. Combination of an AOD or resonant scanner with a piezoelectric actuator allows for high-speed 3D imaging (see below), while highly sensitive GaAsP detectors with negative dispersion allow for minimal laser dose applied to biological samples, a critical feature for relatively long-term acquisitions with no photo-damage. The laser power was varied based on the depth of the cell and imaging conditions, but in general, we used 3-4 mW for slices, and between 9-20 mW *in vivo*, depending on depth and cranial window condition, measured exiting the objective.

Experiments in brain slices were performed at 34˚C under constant aCSF flow. In hippocampal experiments, astrocytes were imaged in the CA1 (stratum radiatum) and DG (medial and outer molecular layers) regions. Cells with soma positioned 30-50 µm below the slice surface were selected for imaging based on their healthy appearance (revealed by SR101), isolation from other GCaMP6f-expressing astrocytes and low basal calcium signal (revealed by GCaMP6f). In whole cell experiments, to image the entire astrocyte over time, an appropriate bounding cuboid was selected for each cell, whose volume (the volume of interest, VOI) depended on the actual size and shape of the specific cell under investigation revealed by SR101. VOI covered an imaging volume of (xyz range): 45-55 µm x 45-50 µm x 28 µm with 0.129-0.144 µm lateral resolution and 1µm axial resolution. In fast 3D experiments smaller VOI were centered on specific cell regions of interest (e.g., processes or end-feet). In these experiments, the average size of an imaged VOI was (xyz) 30 µm x 22 µm x 8 µm for processes, and 35 µm x 25 µm x 8 µm for end-feet. For cortical slice experiments, astrocytes were selected from the somatosensory region at a position and depth comparable to those of the experiments *in vivo* (see below for details). Imaging parameters, including acquisition rate and dimension of VOI, were also comparable to those used in imaging experiments *in vivo* and in hippocampal slices. For axonal stimulation experiments,

somewhat larger volumes were selected (typically 120 x 70 x 25 µm) at the expense of lateral resolution (0.2-0.3 µm per voxel). 3D + time images of single astrocytes were normally acquired at 2Hz (range: 1.5-2.2), i.e. with 28 individual two-photon focal planes scanned every 500 msec. In some experiments, the scanned volume was reduced and the acquisition rate increased up to 10 Hz. Typically, two 3 min-long acquisitions were made for each cell, spaced by 1 min interval, allowing for drift correction if needed. Two control measures were performed to exclude that significant photo-damage or induction of $Ca^{2+}$ activity by laser occurred during our acquisitions: (a) comparison of mean frequency of the $Ca^{2+}$ activity between runs 1 and 2, which showed no difference (P=0.44; paired t-test, n=14 cells); (b) check of whether overall GCaMP6f fluorescence intensity in the VOI slowly increased during acquisition periods, which also gave negative result. In some experiments the effect of Tetrodotoxin (TTX, 1 µM) was tested. The drug was bath applied for at least 10 min prior to recording (perfusion speed: 2ml/min). In these cases, two control runs were performed followed by the run in the presence of the drug. In other experiments, the effect of 4-aminopyridine (4-AP, 100 µM) was tested. The drug was bath applied for 10-15 min. Neuronal activity was monitored in parallel to astrocyte 3D $Ca^{2+}$ dynamics, through a glass pipette electrode (resistance 5-8 MΩ when filled with aCSF) placed 20-30 µm away from the imaged astrocyte. Field signals were amplified, digitized at 20 kHz, and bandpass-filtered at 0.01- 80 Hz. The resulting trace was superimposed to the astrocyte $Ca^{2+}$ imaging traces. For axonal stimulation experiments, the recording duration was increased to 15 min per acquisition (see below), and an additional 15 min-long recording was added for the TTX experiments.

Experiments in head-fixed awake mice were performed in the somatosensory cortex. Astrocytes were imaged at least 80 µm under the brain surface, and camera tracking of movements was generally combined. Similar to the experiments in brain slices, VOI covered an imaging volume of (xyz range): 36-43 µm x 36-43 µm x 20-35 µm with 0.121-0.144 µm lateral resolution and 1 µm axial resolution. Scanning rate was 1-3.3 Hz. The same astrocyte was imaged for 3-5 min (250-600 stacks) and, after 1 min of break, again for 3-5 min. Like in experiments *in situ*, we found no evidence of an increase in the frequency of $Ca^{2+}$ events between run 1 and 2 in any of the analyzed astrocytic regions (soma: P=0.4; processes: P=0.9; end-feet: P=0.9; n=3 cells). In addition, no slow increase in fluorescence intensity throughout the GCaMP6f channel was observed during the time series. In the experiments conducted under anesthesia, isoflurane (2%) was administered in $O_2$. In a few experiments, the same cell was imaged before and after isoflurane administration.

3D $Ca^{2+}$ imaging data analysis

The big data generated by 3D two-photon imaging (3-7GB per acquired cell) were processed thanks to the in house development of a dedicated analytic framework written in MATLAB for analysis and requiring Imaris 8.2 for visualization. To start, when drift was present, correction in xyz (3D translations) was performed taking into account the morphological channel (SR101 stacks) and using a mean square error minimization approach. The same transformation was consequently applied on the other channels. For acquisitions *in vivo*, recording time with movement >1 µm axial or in y-x, usually seen as a peak or a drop in the SR101 morphological signal, was excluded from analysis. If movement was limited to 1 or few frames, $Ca^{2+}$ events in that period were considered empirically (e.g., counted for frequency measures but excluded from more precise measures, such as maximal volume spread). In order to reconstruct as much precisely

as possible the 3D structure of each recorded astrocyte, average time projections of both SR101 and GCaMP6f fluorescence were used for segmentation. In particular, SR101 time projection revealed accurately the structural "core" of the astrocyte, whereas GCaMP6f time projection revealed all the calcium-active parts of the astrocyte during the recording period, including the gliapil. Quality of the time projection was confirmed by comparison with high signal-to-noise, high-resolution z-stacks that were acquired at the end of every $Ca^{2+}$ imaging session. Segmentation of each isolated astrocyte was performed by keeping all the voxels with intensity higher than average background value obtained from VOI regions devoid of any astrocytic structure. The structural core of the astrocyte was separated from the gliapil by using semi-automatic thresholding, based on 3D connected filters under user supervision, and further sub-divided in macro-regions: soma, stem processes with their structurally-resolved (≥1 µm) appendages, end-feet. $Ca^{2+}$ signals in the structural core of the astrocyte were extracted via what we called the "core segmentation method". The core structure was automatically divided into sub-regions (SR) using a 3D geodesic distance of 1 to 3µm of increment, depending on the experimental dataset (in particular, 1 µm increments were used for fast end-feet imaging, and 3 µm steps in all the other experiments). In every SR, ΔF/F calcium signals were computed as the spatial mean intensity at each different time point (FSR(t)) subtracted by the mean (mSR) of FSR(t), and normalized by mSR: (FSR(t)- mSR)/mSR). $Ca^{2+}$ events were automatically detected, under user supervision, by means of the dynamics of regional maxima to detect peaks in every trace independently (*14*). Peaks of two contiguous SRs were automatically assembled into larger $Ca^{2+}$ events based on their 3D connectivity and if they occurred within <3s one from the other. For each event, amplitude (from baseline to peak), duration (full-width half-maximum, FWHM), rise- time (from 10% to 90% of the peak amplitude), decay-time (from 90% to 10% of the peak amplitude), spreading distance (number of geodesic SR involved) and maximal volume spreading were automatically extracted and checked by the user. The hotspot event spread (total number of SR involved) was calculated only for those events involving the local hotspot regions of each process, defined as the subregion with the highest number of events detected over the entire recording time. Information about $Ca^{2+}$ events occurring in the core of all the recorded astrocytes was registered in a database allowing rapid extraction of parameters related to events involving specific macro-regions. In practice, the maximum value for all the here-above parameters was used in each SR of a given macro-region involved in an event. As a result, events were classified into spreading versus non-spreading ones. Moreover, events were sub-classified as "fast" or "slow" if their duration in a given macro-region was <1.5s or ≥1.5s (FWHM). Due to the movement issue, this analysis could not be performed comprehensively in cells from the *in vivo* preparation. In order to get quantitative information on the ongoing $Ca^{2+}$ activity throughout the astrocyte, i.e. including also in the structurally unresolved gliapil, we developed a second analysis approach, that we called "structure-free method". 3D $Ca^{2+}$ activity throughout a segmented astrocyte, i.e. in the entirety of voxels having an intensity higher than the average background value, was computed voxel-wise as the frequency of changes of ΔF/F GCaMP6f fluorescence signal above threshold (inactive to active transition of a given voxel). Threshold was fixed in 3 to 4 standard deviations for experiments in situ and in 2 to 3 standard deviations for experiments *in vivo*. In some experiments, this was preceded by Gaussian filtering in time (1σ) and followed by spatial rescaling at 1µm per voxel in xyz with tricubic interpolation (see below). Data were expressed as mean voxel frequency. First, voxel frequency was calculated for each individual voxel, by dividing the number of inactive to active transitions of the voxel by

the duration of the recording period. Mean voxel frequency was then calculated as the mean of all the individual voxel frequency values in the segmented astrocyte. Mean voxel frequency values were obtained also for specific macro-regions/compartments (core, gliapil, soma, processes, and end-feet) by averaging individual voxel frequencies in the specific macro-region of interest. Comparison of mean voxel frequencies in core and gliapil required normalization by volume fraction because of the different nature, homogenous (core) versus spongy (gliapil), of the two macro-regions (see Ref. (*52*) and method of morphometric analysis). Additional analyses were performed to address specific aspects of the study by use of either one of the two methods or a combination of them. Estimation of the % of the total 3D $Ca^{2+}$ activity in an astrocyte that would be reported by a single two photon focal plane (1 μm) was calculated by dividing the mean voxel frequency in the given focal plane by the mean voxel frequency in the full astrocyte. For this comparison, the best 2D focal plane was selected, defined as the focal plane including the highest amount of astrocytic activity. $Ca^{2+}$ event frequencies in the astrocyte core were classified based on the macro-region/compartment of the event into process, end-foot and soma. Events spatially spreading in two or more macro-regions (processes count individually) were counted 1 in each of the macro-regions. The number of events attributed to a given macro-region was expressed as % of the total number of events counted in all the macro-regions during the acquisition time. Comparison of event frequencies in the different macro-regions in astrocytes of hippocampal slices versus cortical astrocytes *in vivo* required normalization of frequencies per number of subregions in processes and number of end-feet (size being more homogeneous for end-feet) recorded in the two preparations. Distribution of $Ca^{2+}$ activity in each process was obtained by rescaling at 1μm per voxel in xyz and extracting the activity value (voxel frequency) for each voxel together with its 3D geodesic distance from the soma. By this, the activity level every 1μm away from the soma could be reconstructed and used to identify the average size of hot and cold regions within each process. In parallel, the % of process volume expressing a given activity level was calculated. Maximal volume spread and total duration of $Ca^{2+}$ events involving the somatic region were extracted with the structure-free method upon spatial rescaling at 1μm per voxel in xyz. To calculate the volume, we considered the sum of the total number of spatially connected active voxels involved in each event; to estimate the total volume of global events *in vivo*, gliapil volume was corrected by volume fraction. To calculate the duration, the total active period from the start (first active voxel/s) to the end of each event (last active voxel/s) was considered. Study of synchronicity of the activity between two end-feet or between an end- foot and its process was performed by considering the peak amplitude of two $Ca^{2+}$ events in the two different regions: if their peaks occurred <3 seconds apart, the two events were considered as synchronous. In addition, for the coordinated activity between an end-foot and its process, events needed to occur in anatomical continuity.

"Lead-lag" time delay correlation analysis

To understand the spatio-temporal evolution of "global" $Ca^{2+}$ events, GCaMP6f-expressing astrocytes were recorded *in vivo* at high speed but lower voxel count (generally by reducing the number of z-planes). Next, a temporal cross-correlation was performed on the $Ca^{2+}$ traces extracted from each voxel, vs the average $Ca^{2+}$ activity across the entire volume containing the global $Ca^{2+}$ event. This was used to assign a temporal delay value to each voxel as compared to the global population. Next, each voxel was color-coded according to the relative time offset of the lag bin

with the maximum cross-correlation value and assigned either to the "leader" or the "lagger" category. For lead-lag analysis on global events, neighborhood cross-correlation was normalized by subtracting the means of both the voxel and the global-average traces, and diving by their standard deviations. Unlike for the electrical cumulative cross-correlation calculation (see below), the individual time lag bins were not averaged. In a few cases, we have applied additional threshold, discarding any voxel whose maximum bin correlation was below an arbitrary value (e.g. 0.20): this resulted in larger fragmentation ("patchiness") of the maps, but did not produce a qualitative change in the spatial distribution of the lead/lag zones around the astrocyte, and is therefore not presented.

Axonal stimulation experiments

$Ca^{2+}$ responses in DG astrocytes were evoked via targeted threshold stimulation of fluorescent (tdTomato or jRCaMP1a) PP axons. Brief current pulses (100-300 μs, 30 μA) were delivered focally to segments of the axons via a monopolar glass electrode (patch pipette, 4-6 MΩ when filled with aCSF) with the tip covered by fluorescent Quantum Dots (*53*), positioned ≥40 μm away from the imaged astrocyte to avoid any direct activation. This stimulation strength typically produces minimal synaptic activation in a postsynaptic neuron (*36, 54*). The axonal stimulation protocol consisted of 1 to 5 pulses (paired at 50 ms), delivered every 20 seconds. To discriminate the evoked and spontaneous $Ca^{2+}$ activity of an astrocyte, stimulation periods (2-3 mins) were interposed with "rest" periods of the same duration. 3D $Ca^{2+}$ data over time were collected at a typical throughput rate of 250 Mbps, corresponding to about 60 GB of data for a typical (30 min) duration of each recording. These $Ca^{2+}$ data were acquired using a commercially available acquisition system externally synchronized to a separate electrophysiology system. The latter performed extracellular field recording and/or axonal stimulation via pClamp/AxoScope 10.3 software driving digitizers linked to the amplifier, constant current stimulator, and also receiving the Y-galvanometer feedback position from the imaging system. The Y-galvo position output pin was sending the 3D + time stack frame count, including the realtime Y-scanline position for each frame, and was continuously sampled at 1 kHz by the electrophysiology setup throughout the experiment. In this fashion, the exact relative timings of each current pulse and each 3D frame were available for correlation analysis. Detection of the stimulation-activated astrocytic $Ca^{2+}$ responding regions in the 3D volume of the astrocyte was accomplished post-hoc via a specially developed ImageJ (NIH) software plugin (available from Volterra lab). Briefly, for each of the 3D voxels, a response index was calculated by performing a modified normalized cumulative cross-correlation between the voxel's $Ca^{2+}$ signal time series and an electrical stimulation trace on a short (4-7 s) lead/lag window. To compensate for the jitter present in the onset of astrocytic $Ca^{2+}$ responses, cross-correlation coefficients for all the positive values of lag were summed up. The corresponding formula for this calculation is as follows:

$$\mathrm{NCCC(x,y,z)} = \frac{1}{w}\sum_{l=0}^{w}\sum_{t=0}^{d-w}\frac{\left(m_{t-l}(x,y,z) - \overline{m}(x,y,z)\right)\cdot\ n_t}{\sigma_{m(x,y,z)}}$$

where CC is the normalized cumulative cross-correlation coefficient for each voxel centered at coordinates (x, y, z), mt is the calcium trace and nt is a binary transform of an electrical stimulator

input at time t, w is the length of the cross-correlation window, and d is the duration of the acquisition in sample points. Following the calculation, the CC values for each voxel were thresholded to indicate the actively time-locked "responding regions" of the astrocytic structure. The responses were verified by placing VOIs and overlaying the extracted $Ca^{2+}$ and input stimulator traces. Furthermore, when the image data were cross-correlated to the "scrambled" electrical input trace, this produced a much lower number of significantly correlated voxels (Fig. S11A). For the dual $Ca^{2+}$ indicator experiments (Fig. 7C), we expressed jRCAMP1a in PP axons, and GCaMP6f in astrocytes. Both fluorophores were simultaneously excited at 965 nm, and the acquired red and green signals were analyzed in ImageJ. Because axonal $Ca^{2+}$ transients were weaker, this necessitated a larger oblong VOIs traced along a short stretch of the putatively activated axon, placed immediately adjacent to the astrocytic VOI. To maximize effective $\Delta F/F$ for jRCaMP1a, we reduced background slice fluorescence by omitting incubation with red morphological dye SR101 prior to functional $Ca^{2+}$ measurements, but instead visualized astrocytic morphology by post-loading the slice with a higher SR101 concentration via a perfusion system at the end of the recording (500 nM solution perfused at 3 mL/min at 34 °C, for 20 minutes).

In a set of control experiments, we evaluated the neuronal responses to axonal stimulations using protocols identical to those of the astrocyte experiments. In particular, we evaluated the percentage of neuropil volume that responded to axonal activation. Mice carrying the floxed GCaMP6f gene were injected with a neuronally-targeted AAV5.CamKII:Cre virus, leading to neuronal expression of the $Ca^{2+}$ indicator. The relative size of the responding neuropil regions was calculated as done for the reliably responding regions of astrocytes. For experiment in Fig. S10B, two HFS pulses were added to the stimulation protocol to weakly highlight the general direction of the maximally-reachable neuropil regions.

3D morphometric analysis

Acute brain slices from P30-P40 *GFAP-EGFP* mice (*45*) were imaged with two-photon setup 2 at a resolution of 0.05 x 0.05 x 0.5 $\mu m^3$ (xyz) over 50-80 µm, axially centered on a given astrocyte in order to acquire its entire structure. Only EGFP-expressing astrocytes not surrounded by any other fluorescent astrocyte and therefore displaying an unambiguously identifiable structure were selected. Three-dimensional images of the astrocytes acquired in the CA1, CA3, DG hippocampal regions and in the somatosensory cortex were analyzed with custom made programs written in MATLAB (MathWorks Natick MA USA), and visualized with Imaris 8.2 (Bitplane, Switzerland). EGFP-expressing astrocytes were segmented by keeping the voxels having an intensity higher than the average background value (i.e. where there was no astrocytic structure). The structural core part of the astrocyte, including cell soma, end-feet and stem processes with appendages up to structural elements ≥1 µm that could be visually identified at optical resolution, was separated from the structurally unresolved gliapil by using semi-automatic thresholding under user supervision, allowing to define the soma, main processes and end-feet. Gliapil was defined as the segmented astrocytic parts which were not in the core. Gliapil volume was corrected by volume fraction (VF) from the core (*52*). Thus, the intensity value of each voxel within the gliapil was divided by the average intensity within the core to obtain the VF for all the voxels. The volumes were defined as the sum of all the VF of all the voxels within the core (containing 100% of astrocytic structure: VF =1) and gliapil multiplied by the physical size of a voxel. For each 2D vs 3D comparison, the "best 2D" focal plane, i.e. the plane containing either the biggest amount of

astrocytic structure, or the biggest number of end-feet or processes, or the longest process length (calculated as the longest path amongst all the possible bifurcations from the soma to the smallest resolvable branch), was automatically found in every possible slice of 1μm thickness and divided by the corresponding total quantity in 3D. For morphometric quantification of axonal linearity, images of individual tdTomato-fluorescent PP fibers in the hippocampal DG were acquired using VOIs with increased lateral (up to ~0.06 μm) and axial (0.5 μm) resolution and temporal averaging. Axonal fibers were semi-automatically traced in xy and lz projections using NeuronJ plugin (*55*) and a custom written ImageJ script. The resulting 3D coordinate files were analyzed for lateral and vertical deviation from the principle layer (bulk) fiber direction. For cases of high fiber density, individual fiber signals were pre-segmented in 3D using a custom ImageJ plugin before tracing (available from Volterra lab).

Statistics

For all statistical analyses, Matlab, Origin 8, GraphPad Prism 6, and Excel were used. Data were generally expressed as mean value ± SEM and considered as significantly different when the p value was less than 0.05. Unpaired t-tests or rank sum test were used when comparing the means of two independent experimental populations (e.g. properties of Ca2+ events such as duration, or categories, data ex vivo vs. in vivo), whereas paired t-test or signed rank test were used for comparing interdependent populations (e.g., Ca2+ activity between runs 1 and 2, events in 2Hz and 10 Hz acquisitions). For 3D morphometry statistical comparisons were made using paired non parametric Kruskal-Wallis' test or with Wilcoxon rank sum test, depending on the type of comparison.

**Table S1. Properties of the $Ca^{2+}$ events detected in the core regions of GCaMP6f-expressing astrocytes in acute hippocampal slices*.**

| Astrocyte Region † | Amplitude (ΔF/F) | Duration (FWHM, s) | Rise time (s) | Decay time (s) | Volume ($\mu m^3$) § | Spreading distance ¶ | N-value (events) |
|---|---|---|---|---|---|---|---|
| Processes | 2.33 ±0.05 | 2.64 ±0.07 | 2.58 ±0.10 | 4.33 ±0.19 | 47.93 ±2.08 | 2.11 ±0.06 | 567 |
| End-feet | 1.93 ±0.14 | 2.94 ±0.28 | 2.36 ±0.29 | 4.53 ±0.73 | 90.77 ±12.88 | 1.66 ±0.13 | 65 |
| Soma | 2.18 ±0.27 | 5.13 ±0.44 | 4.50 ±0.46 | 8.16 ±1.17 | 478.51 ±17.99 | 4.91 ±0.31 | 34 |

* $Ca^{2+}$ events detected using GCaMP6f as indicator, 2Hz as speed of volumetric 3D two-photon imaging acquisitions and analysis performed with "core segmentation method" as described in Methods. Care should be taken when comparing the event parameters reported in this Table to those obtained in other studies using different acquisition modes (e.g., incomplete 2D/confocal), different $Ca^{2+}$ sensors (e.g. slower GCaMP3/mGCaMP3), different acquisition speeds (much slower or faster than 2 Hz), and different analysis approaches.

† Astrocytic regions defined by segmentation of the astrocytic core according to live SR101 staining. Within regions, sub-regions defined by segmentation of the region in equal geodesic distance increments away from the center of the soma, step size: 3 μm.

§ $Ca^{2+}$ event volume is calculated as the total volume of all the individual sub-regions involved in the event. Please note that these values have a "quantal" resolution of one sub-region, and true event volumes may in reality be smaller as an event could occupy just portions of its extreme sub-regions. Also, notice that average sub-region volumes are different in different astrocytic regions: 21.14± 0.73 $\mu m^3$ in processes, 51.75± 6.64 $\mu m^3$ in end-feet, 83.90±7.05 $\mu m^3$ in soma. End-feet sub-region volumes overestimate real volumes because the SR101 signal does not permit exact dissection of the end-foot enwrapping a vessel from the vessel structure itself.

¶ Spreading distance is defined as the number of contiguous sub-regions involved in each event. For soma, sub-regions were defined as "tangerine" segments.

Abbreviations: FWHM, full width duration at half-maximum amplitude; s, seconds,

**Supplemental Figures S1-S11:**

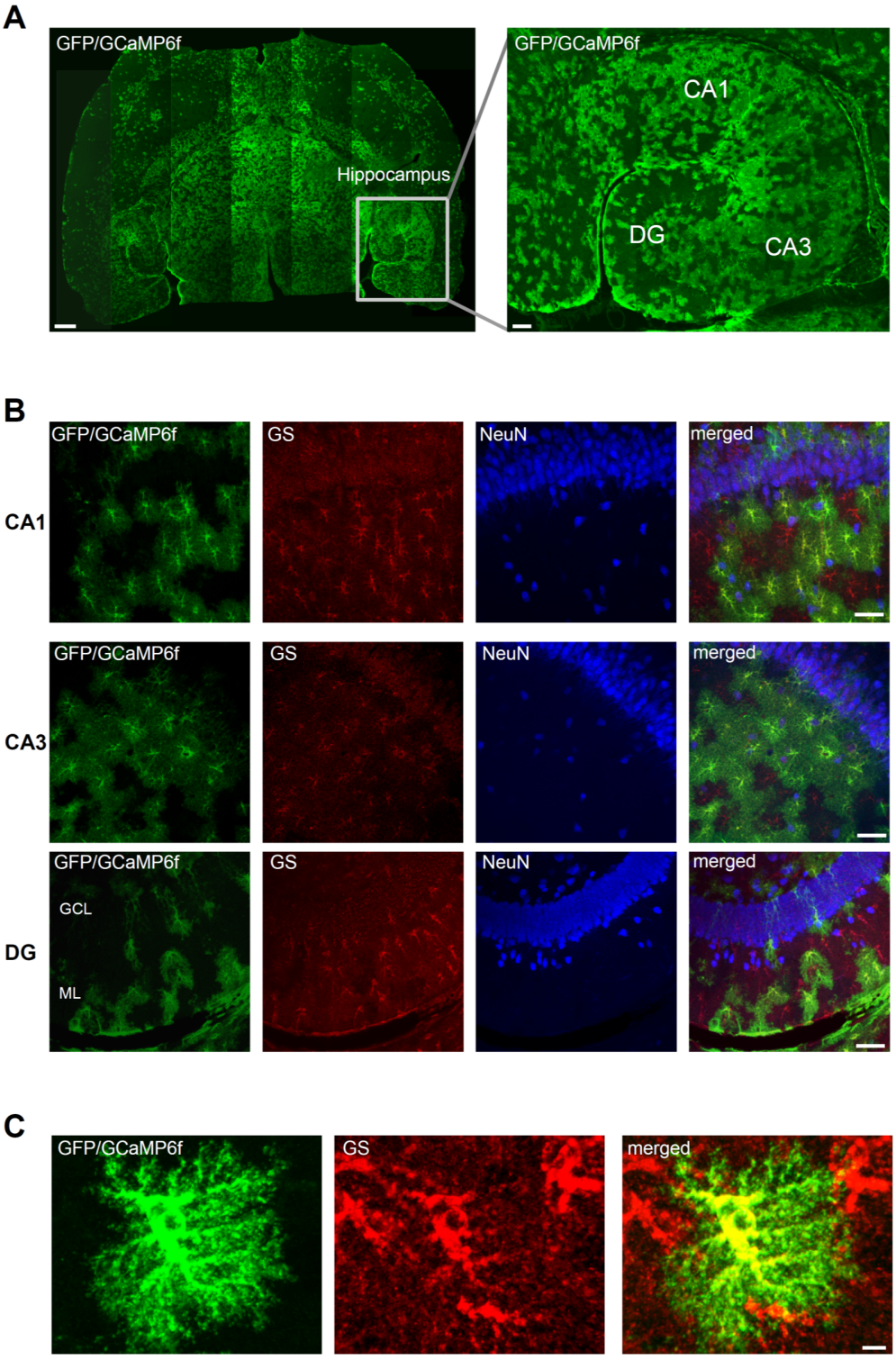

**Fig. S1. Characterization of *GFAPCreERT2xGCaMP6f* mice with immunohistochemistry.**
**(A)** *Left*: 7x5 combined confocal images show the horizontal brain section of a 39 days-old mouse taken 15 days after the first tamoxifen injection. GCaMP6f expression is present throughout the brain (green, GFP/GCaMP6f: GCaMP6f labeled with anti-GFP antibody). Scale bar: 500 μm. *Right*: zoom-in of the hippocampal region shows patchy distribution of GCaMP6f expression hinting already to an astrocyte-specific pattern (DG: dentate gyrus; CA1 and CA3: cornu ammonis 1 and 3). Scale bar: 100 μm. **(B)** Astrocyte-specific expression of GCaMP6f in the CA1, CA3 and DG hippocampal regions. From left to right, staining with: GFP for GCaMP6f (green), glutamine synthetase (GS, red) as astrocyte marker, NeuN (blue) as neuronal marker, and overlay of the three (maximum intensity z-projection from four to eight 1μm-thick confocal stack acquisitions; scale bar: 50 μm). Astrocyte-specificity is 100% in CA1 and CA3 (n=79 cells in CA1; 97 in CA3), whereas is 90% in DG (n= 90 cells), where a minor population of neural precursors/immature neurons (9 cells neither GS-positive nor NeuN-positive and 1 cell NeuN-positive) are labeled together with astrocytes. **(C)** GFP labelling reveals homogeneous and widespread GCaMP6f expression throughout the structure of an astrocyte. From left to right: 3D view of a 29μm confocal stack of an astrocyte as revealed by GFP/GCaMP6 labeling (green), GS labeling (red) and their overlay. The GECI expression seen in this astrocyte in isolation from neighboring ones, covers the astrocyte volume beyond the structures revealed by GS staining and is therefore valid for reporting Ca2+-activity from throughout the astrocyte, including the optically less resolved regions like the gliapil. Scale bar: 5 μm.

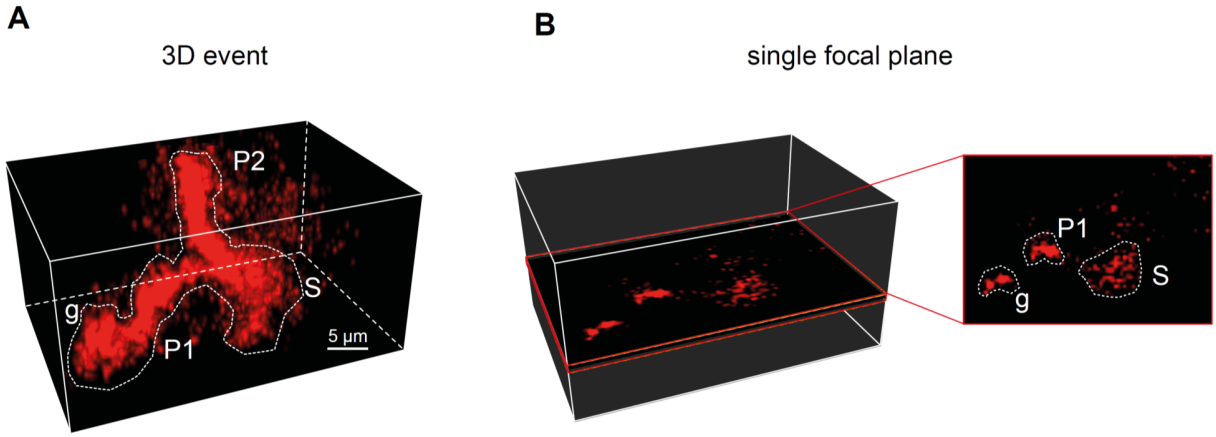


**Fig. S2. Incorrect detection by 2D imaging of astrocytic Ca2+ events spatially spreading over multiple focal planes.**

**(A)** In red, reconstruction of a complex three-dimensional $Ca^{2+}$ event encompassing two processes (P1, P2), the soma (S), and parts of the gliapil (g). The event spreads over multiple focal planes (dimension of imaged VOI: 42 x 28 x 21 µm). **(B)** This single event would be incorrectly reported by 2D imaging in a single focal plane, even in the best plane: first, the event would be seen as three smaller unconnected events, one in the gliapil, another one in P1 and a third one in the soma, with errors in both event frequency and spatial spread. Second, the parts of the event spreading to the second process (P2) would be entirely missed with a further error in the spatial spread of the event.

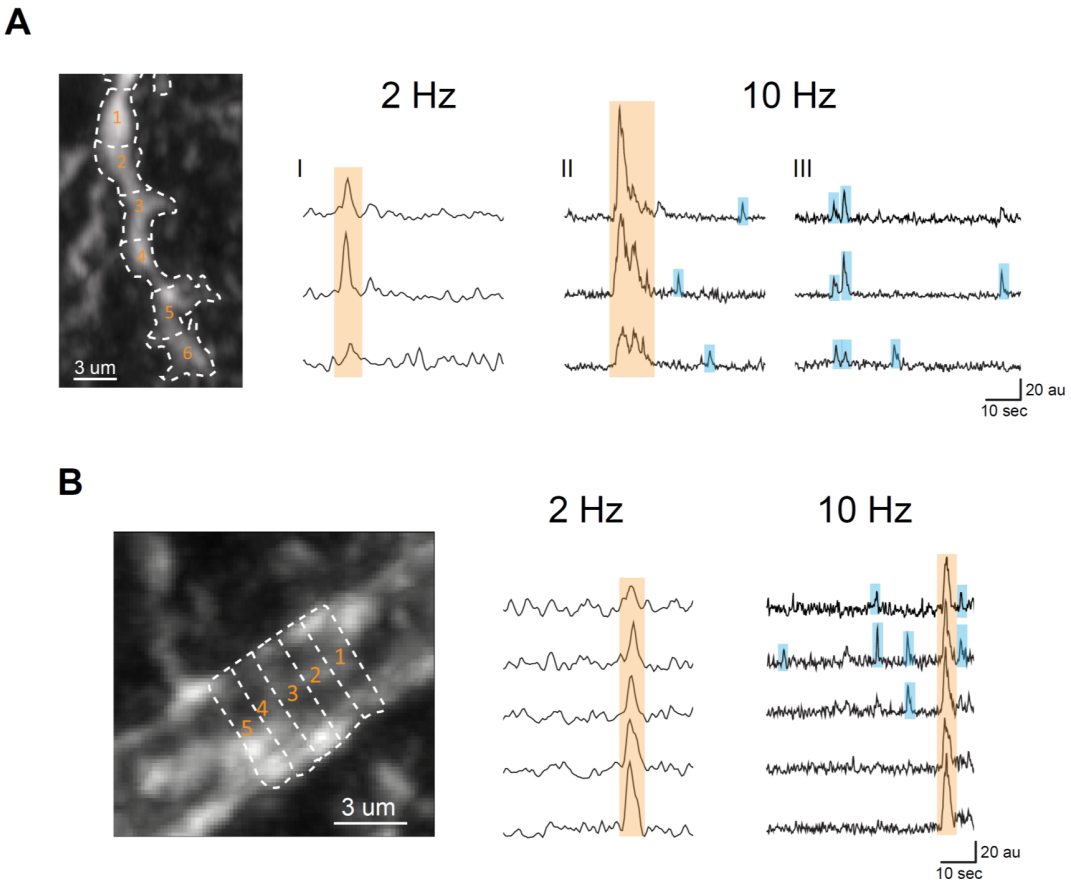


**Fig. S3.Increasing 3D acquisition rate permits detection of faster $Ca^{2+}$ events in astrocytic processes and end-feet.**

**(A)** $Ca^{2+}$ activity detected in a single process imaged in 3D at either 2 Hz or 10 Hz. The core structure of the process is revealed by SR101 loading (in grey, time projection over the whole imaging period) and, in both types of acquisition, is segmented in consecutive sub-regions of 3 µm length (1-6). $Ca^{2+}$ traces from groups of neighboring sub-regions (SR) are shown (group I = SR 2-4, starting from the top trace; II = SR 3-5; III = SR 4-6). For each group, $Ca^{2+}$ traces were selected by cropping representative stretches of activity during acquisitions recorded at either 2 Hz (group I) or 10 Hz (groups II and III). Events are highlighted with different color-codes according to their features. $Ca^{2+}$ events with duration ≥1.5 sec (FWHM, orange highlight) were captured at both 2 Hz and 10 Hz, but sampling at 10 Hz revealed the additional presence of a population of faster and smaller events, often restricted to one or few SRs (light blue). **(B)** $Ca^{2+}$ activity detected in an end-foot imaged at either 2 Hz or 10 Hz. The end-foot structure is revealed by a combination of SR101 and GCaMP6f signals projected over the entire recording time and divided in consecutive sub-regions of 1µm length (1-5). $Ca^{2+}$ traces from each of the 5 sub-regions during the 2 Hz and 10 Hz acquisitions are comparatively shown and fast and slow events are highlighted with the same color code as in (A). Slow events, visible at both 2Hz and 10 Hz, occupy most of the end-foot structure, whereas fast events, revealed only at 10 Hz, remain confined to just one or few sub-regions, i.e. to fractions of an individual end-foot.

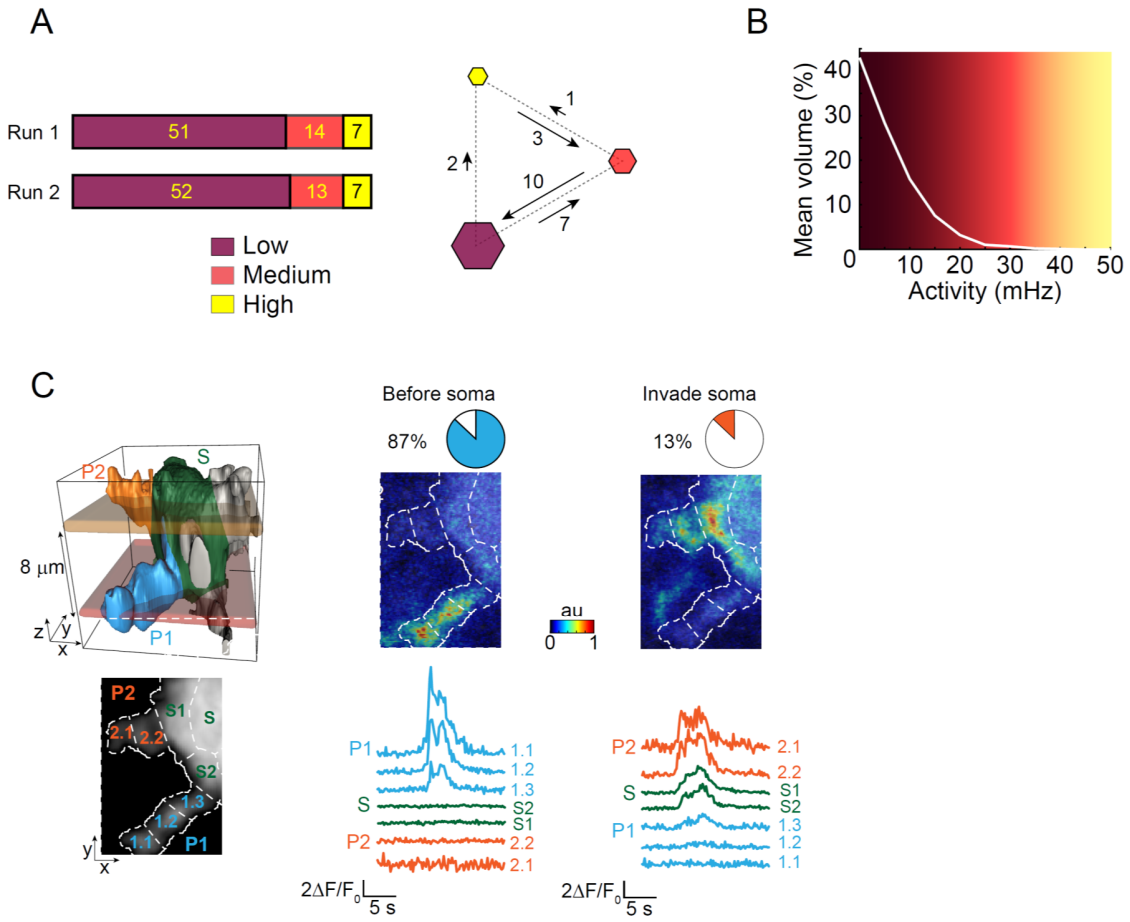


**Fig. S4. $Ca^{2+}$activity in astrocytic processes: analysis of stability over time, frequency per process volume, and likelihood of somatic spread.**

**(A)** Analysis of stability over time. *Left:* Bars show the total number of low, medium, and high activity processes (see Fig. 4A) in two consecutive 3 min-periods of recording (runs). Proportions remained basically the same in Run1 and Run 2. *Right*: number of individual processes that transitioned between activity levels (same color coding than on the left): transitions are indicated by the numbers adjacent to each arrow (e.g., in the second run, 7 processes went from the low to the medium level, whereas 10 other processes went from the medium to the low activity level). **(B)** Graph showing distribution of activity (in frequency) with respect to process volume (in %). Frequency is calculated in 1 $\mu m^3$ domains in every analyzed process (see Fig. 4C,D). **(C)** Likelihood of somatic spread of $Ca^{2+}$ events originating in astrocytic processes. *Left, top:* representative morphological reconstruction of an astrocyte in which we performed 3D monitoring of activity in two processes (P1 and P2) adjacent to the soma (S). *Bottom:* all the P1, P2 and S sub-regions from which we monitored activity. *Middle:* pseudo-color example and corresponding traces of an event in P1 that terminates at the interface with S. *Right:* example of an event in P2 that enters the soma but does not spread from this beyond the interface with P1. These experiments revealed that most of the process events terminate in the interface region before the soma, and only a minority actually invades at least one somatic region.

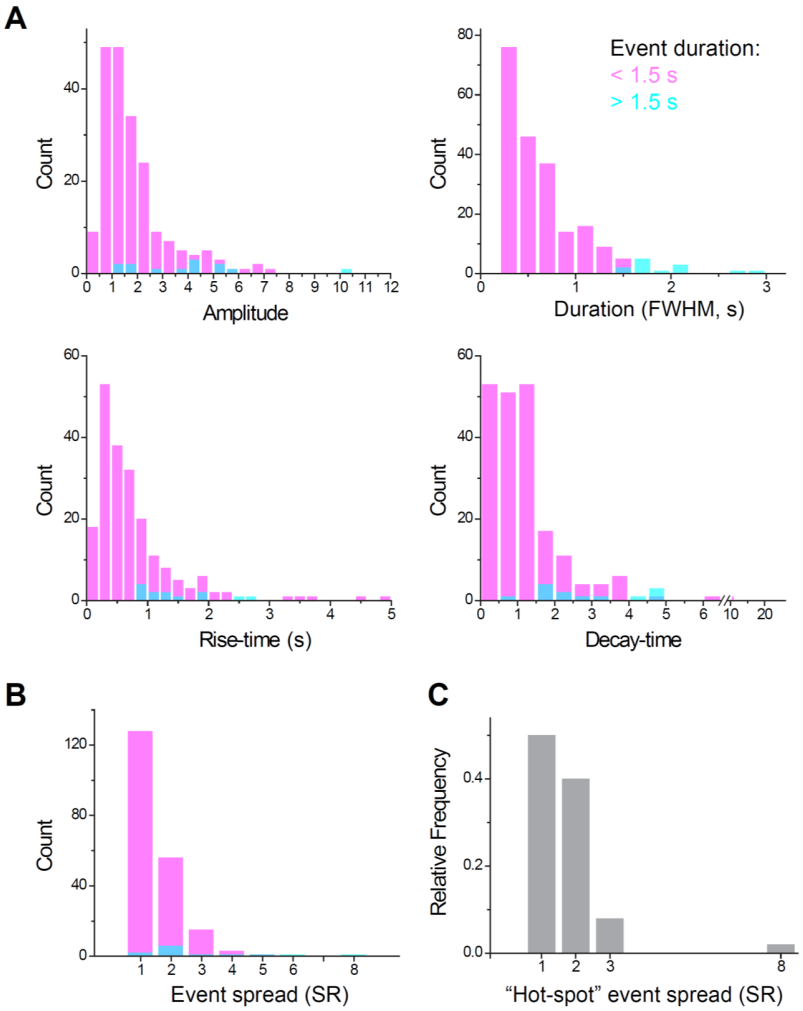


**Fig. S5. Fast-rate volumetric 3D scanning in astrocytic processes: distribution analysis of the $Ca^{2+}$ event parameters.**

In these experiments, the sampled volume was reduced (in z-depth and linear dimensions) to contain just an individual process (see Results); the sampling rate was correspondingly increased to 10 Hz. These experimental conditions revealed the presence of a prevalent sub-population of fast and small $Ca^{2+}$ events not captured in routine 2Hz acquisitions. Analysis performed on 216 $Ca^{2+}$ events from 8 processes in 4 cells. **(A)** Distribution of event properties (amplitude, duration, rise- and decay-time). Magenta color-code denotes "fast" events (FWHM: <1.5s), and cyan "slow" events (FWHM: >1.5s). **(B)** Distribution of spatial event properties. Event spread expressed as number of individual sub-regions (SRs) involved in the event (SRs drawn geodesically along the principal process axis away from soma, in 3 µm increments; average SR volume: 26.17± 2.28 $\mu m^3$). Most events were confined to 1 or 2 SRs; **(C)** Spatial event properties, but restricted to $Ca^{2+}$ events occurring in the "hot-spot" region of each process, i.e. the region showing highest event frequency (see Fig. 4D). Like events in other regions, "hot-spot" events were mostly confined to 1 or 2 SRs, with a somewhat higher percentage of 2 SRs events.

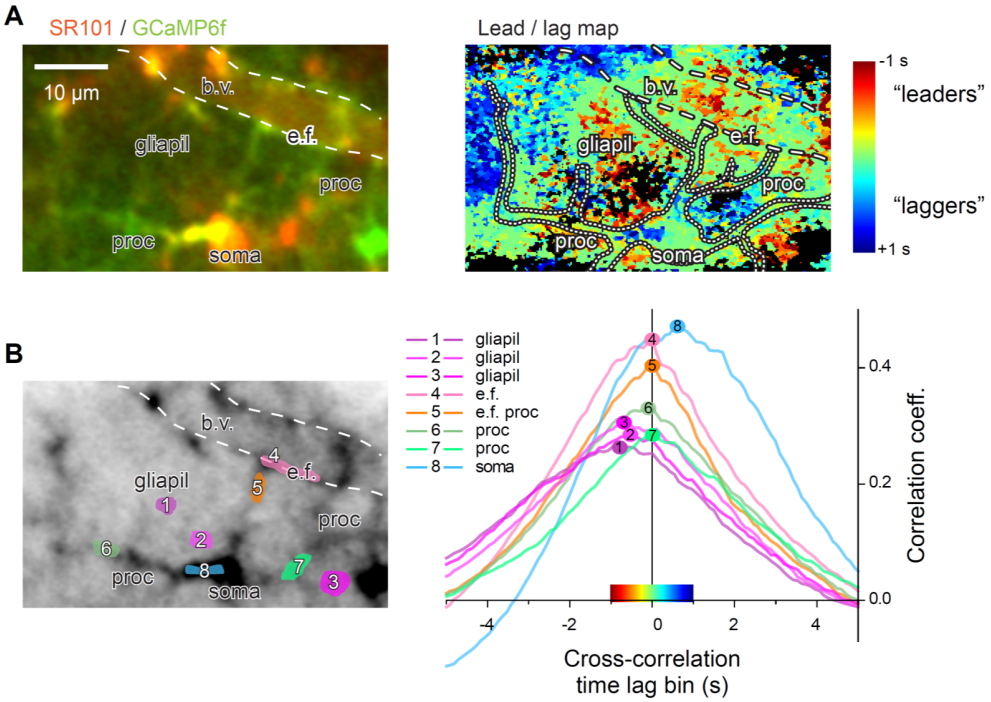


**Fig. S6. Lead-lag cross-correlation analysis of astrocytic $Ca^{2+}$ signals reveals multifocal decentralized nature of global events *in vivo*.**

To study the temporal sequence of fast-developing "global" events *in vivo*, we recorded in few experiments selected parts of GCaMP6f-expressing astrocytes (7 continuous z-frames) at high temporal resolution (10 Hz) and performed a voxel-wise normalized cross-correlation analysis vs the entire event GCaMP6f signal (see Methods). **(A)** *Left:* combined morphological (SR101) and cumulative GCaMP6 signals showing visible components of the imaged astrocyte, including soma, two generic processes (proc), an end-foot process terminating in an end-foot (e.f) contacting a blood vessel (b.v) and the surrounding gliapil. *Right*: normalized cross-correlation projection map wherein individual voxels are colored according to the temporal offset with respect to the time showing the strongest correlation (time lag bin with respect to the greatest correlation value). "Jet" colormap is shown to the side; earliest "leader" voxels are colored in tones of red, latest "lagger" voxels are colored in blue. In general, many small, physically disconnected, regions of gliapil seem to precede the average global event. This suggests a multi-focal origination nature of the "global" events, rather than a "wave" spreading from one side of the cell to another. **(B)** *Left*: gray-scale average GCaMP6f image indicating the placement of the manually drawn VOIs used to extract the average cross-correlation voxel profiles displayed on the right. *Right*: Normalized cross-correlation traces extracted from the voxels in the VOIs to the left. Several areas of the gliapil are "leaders" (VOIs 1-3, pink), and are activated with approximately the same advance despite being physically disconnected in space. Process regions and end-foot activate with minimal offset to the average global event (VOIs 4-7, pink, orange and green), and regions of the soma are significantly delayed (VOI 8, blue, "laggers"). For display purposes, a threshold discarding any voxel with maximum bin correlation <0.20 was applied (voxels below this value are set to black). The same threshold was applied in Fig. 4F.

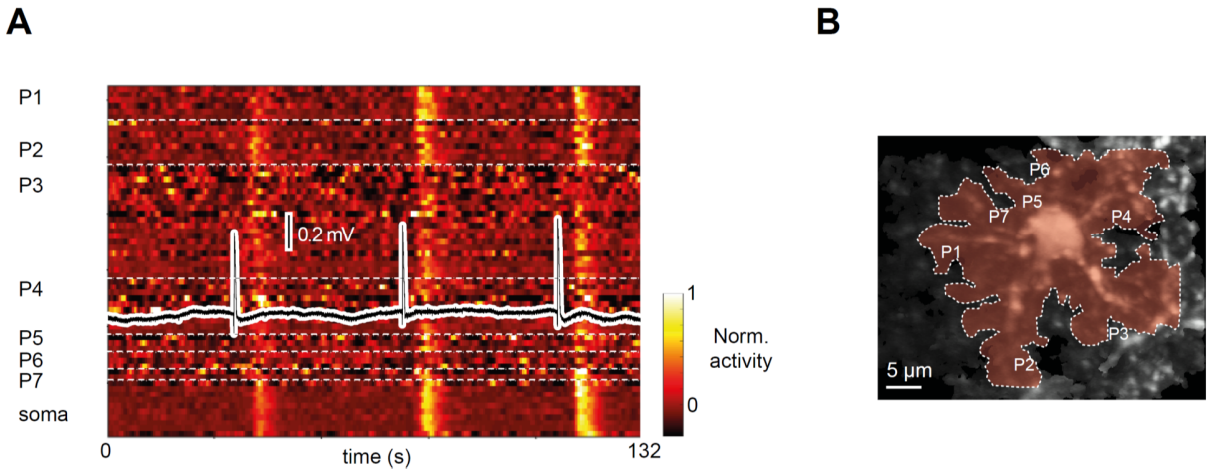


**Fig. S7. Pharmacologically-induced intensified neuronal firing results in "global"-like $Ca^{2+}$ events in hippocampal astrocytes in situ.**

Acute application of the pro-epileptogenic drug 4-aminopyridine (4-AP, 100 µM) results in hypersynchronous neuronal activation in the hippocampus in situ within several minutes of application. **(A)** Representative raster plot of normalized $Ca^{2+}$ activity in all the segmented regions of an astrocyte (P1-P7, processes; S, soma) over about 2 minutes with overlaid synchronized trace of the local field potential (LFP) recorded in the slice. Notice that each large change in the LFP is followed (within 2s) by a "global- like" $Ca^{2+}$ event in the astrocyte. **(B)** Top down view of the same astrocyte visualized by SR101 loading. The overlay indicates the maximum spread of one of the "global"-like events.

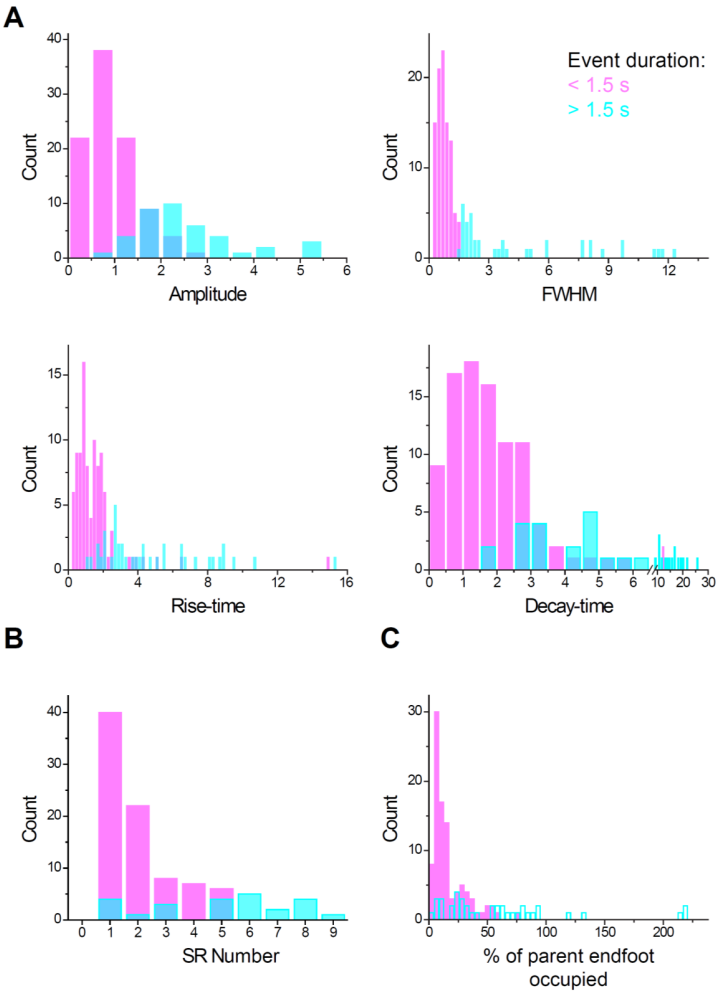


**Fig. S8. Fast-rate volumetric 3D scanning in astrocytic end-feet: distribution analysis of the $Ca^{2+}$ event parameters.**

In these experiments the sampled volume was reduced (in z-depth and linear dimensions) to contain one to three end-feet (see Results); the sampling rate was correspondingly increased to 10 Hz. These experimental conditions revealed the presence of a large sub-population of fast and small $Ca^{2+}$ events, often spatially confined to just a fraction of an end-foot, not captured in routine 2Hz acquisitions. Analysis performed on 136 $Ca^{2+}$ events from 13 end-feet in 4 cells. **(A)** Distribution of event properties (amplitude, duration, rise- and decay-time). Magenta color-code denotes "fast" events (FWHM: <1.5s), and cyan "slow" events (FWHM: >1.5s). **(B)** Distribution of spatial event properties. Event spread expressed as number of adjacent end-foot sub-regions (SRs) involved in the event (SRs segmented orthogonally along the blood vessel in 1 µm steps; average SR volume: 16.99± 0.55 $\mu m^3$. When multiple GCaMP6f-positive end-feet were present contiguously on the same blood vessel, their individual borders were determined visually by the experimenter. **(C)** Distribution of $Ca^{2+}$ event sizes expressed as percentage of the parent end-foot volume. Most events were smaller than an individual end-foot. Values >100% represent synchronous multi-end-foot events.

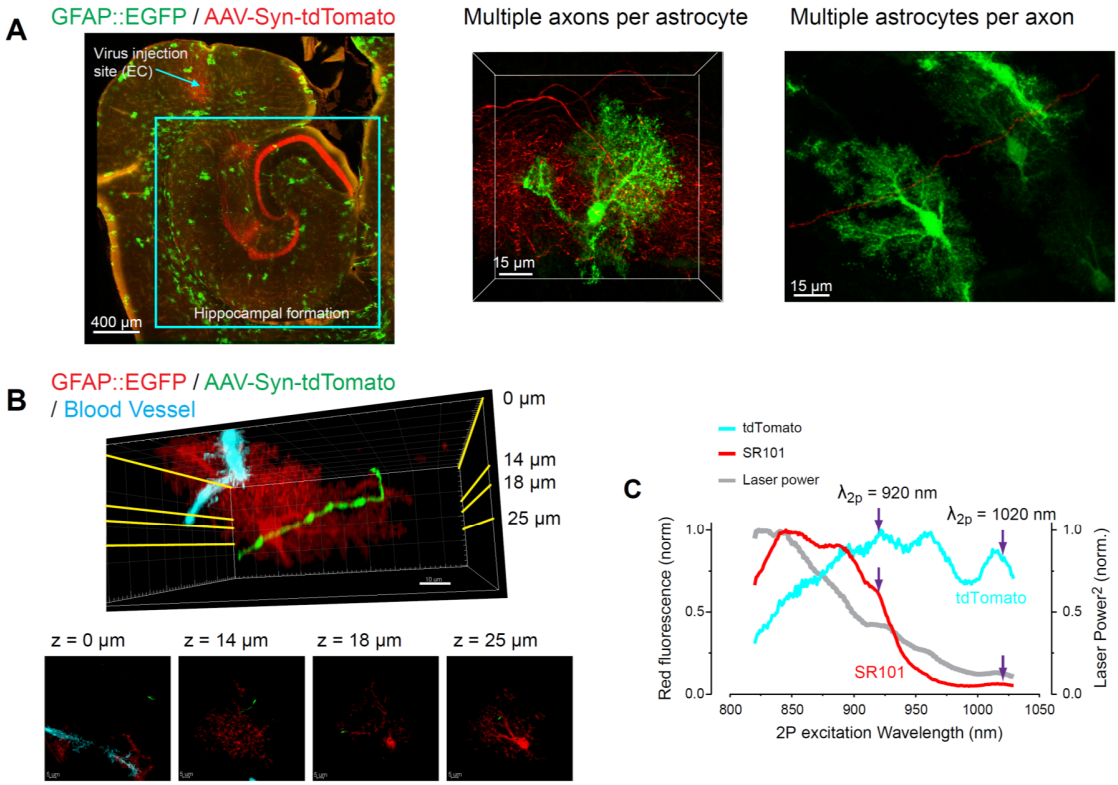


**Fig. S9. 3D study of the complex morphological relationships between axons and astrocytes in the hippocampus.**

**(A)** *Left:* Maximum projection image (45 µm in 9 z-steps) of the forebrain of a *GFAP- EGFP* mouse 4 weeks after injection of AAV-Syn-tdTomato into the entorhinal cortex (EC). Astrocytes are in green, PP axons in red, mostly straight en route (EC, subiculum) and highly convoluted at destination (e.g., DG molecular layer). This dual color approach permitted direct visualization of the complex astrocyte-axon morphological interactions reflecting potential functional interactions, including: *Middle*: multiple axonal fibers crossing a single astrocyte (see also Movie S4); *Right:* a single axonal fiber contacting multiple astrocytes (maximum projection image). **(B)** *Top:* Representative example showing an individual fluorescent axon (green) crossing the 3D territory of an astrocyte (red) and a blood vessel (blue) over multiple focal planes. For clarity, other nearby axons are masked. *Bottom:* the axon-astrocyte interactions as seen from four individual planes. None of them permits to understand the continuity of the morphological (and functional) interactions between this single axon and the astrocytic structures. **(C)** Two-photon excitation spectra of SR101 and tdTomato. To study simultaneously morphological and functional axon-astrocyte interactions in 3D, we used in combination SR101 (loaded at nanomolar concentration in astrocytes) and tdTomato (expressed in axons) in *GFAPCreERT2xGCaMP6f* mice: (see Figs. 6, 7). In spite of similar emission profiles, we could optically separate the two red reporters based on their different two-photon excitation properties. Alternatively, varying wavelengths between 920 (for SR101, left arrows) and 1020 nm (for tdTomato, right arrows), we could unambiguously assign structures to axons or astrocytes without need for any spectral unmixing or similar computational approaches.

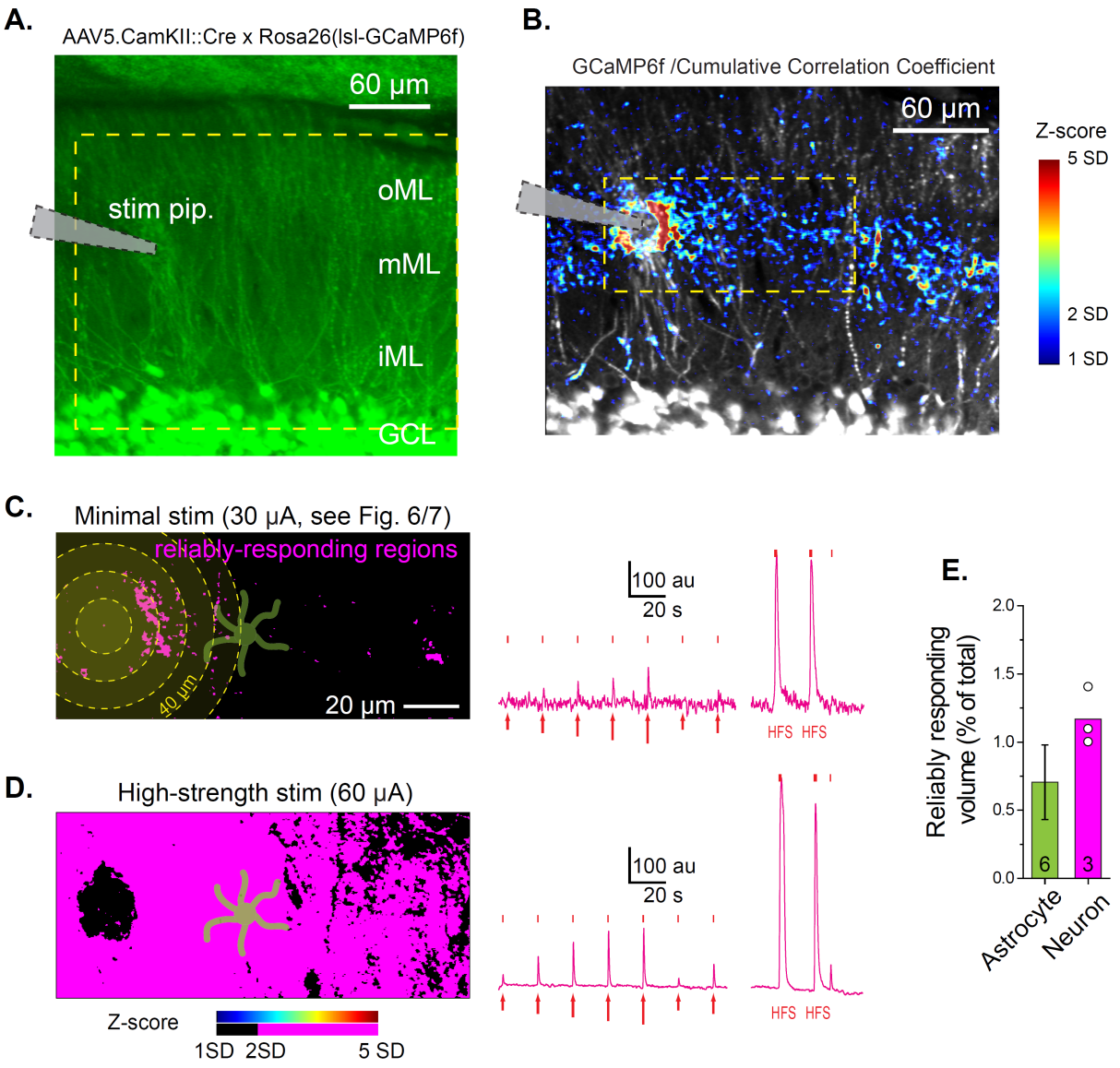


**Fig. S10. Sparse neuronal $Ca^{2+}$ response to minimal electrical stimulation of axons**

Mice with floxed GCaMP6f were injected with neuronal Cre virus (AAV5.CamKII0.4.Cre.SV40) in the dentate gyrus (DG) to trigger GCaMP6f expression selectively in neurons. **(A)** Low-zoom average projection of a two-photon stack illustrating the arrangement for electrical stimulations in the DG. Morphological image processed with a square-root function. Dashed outline indicates the region shown in 2D (z=1µm) in B. (GCL, granule cell layer; o-m-i-ML: outer, medial, and inner molecular layer; stim pip: location of the stimulation pipette). **(B)** Response map produced by 19 "minimal stimulation" episodes (30 µA; 1-5 pulses, see Figs. 6,7 and Methods) augmented by two HFS trains (1s, 100 Hz). Average GCaMP6f signal in grayscale; corresponding cumulative cross-correlation (see Methods) in "Jet" colorscale as indicated to the right. Minimal electrical stimulations produced a low amount of time-correlated postsynaptic responses in the GCaMP6f-

positive regions >20 μm away from the stimulating pipette, visually resembling the expected pattern of axonal divergence in the medial perforant path layer. These sparse but persistent "responding regions" appeared to be the result of activating individual axonal inputs via evoked APs, pre-synaptic release, and post-synaptic activation. In contrast, strongly "responding regions" within ~10-20 μm from the stimulating pipette may be either the result of direct electrical stimulation and/or activation of multiple axons converging onto the same postsynaptic dendrite(s). **(C)** Distribution of the neuronal regions in the DG reliably responding to the protocols in B relative to distance from the stimulating pipette. *Left:* threshold-based ("magenta") cumulative cross-correlation response maps obtained in a single focal plane (z= 1μm) at 70 Hz. An astrocyte is overlaid for illustration purposes, i.e. to show the neuronal $Ca^{2+}$ response in the region typically studied in axon-astrocyte interaction experiments (see Fig. 7). *Right*: Neuronal GCaMP6f signal extracted from reliably-responding regions >40 μm away from the pipette. Responses to minimal stimulation are proportional to the number of pulses (1-5 pulses indicated by arrow size); responses to HFS trains are much larger. Exact timing of each pulse is shown by tick marks above the trace. **(D)** Stronger, "high-strength stimulation" (60 μA) evokes massive time-locked GCaMP6f fluorescence response, 100-fold bigger than threshold stimulation (from 0.83 to 81.66% of the FOV at locations >40 μm), indicating that the small response in C is truly due to sparse neuronal activation, not to lack of GCaMP6f expression in neurons. *Right*: Neuronal GCaMP6f signals extracted from the distal (>40 μm away) reliably responding regions. **(E)** Comparison of the mean astrocytic and neuronal responding volumes to the same minimal axonal stimulation protocol. Experiments in astrocytes and neurons were performed separately. Data are from "before TTX" dataset in Fig. 7 for astrocytes, and from this figure for neurons (n=3 from 2 slices and 2 different animals). Overall, $Ca^{2+}$ responses in both GCaMP6f-positive astrocytes and neurons are sparse and restricted to a minimal fraction of the imaged volume.

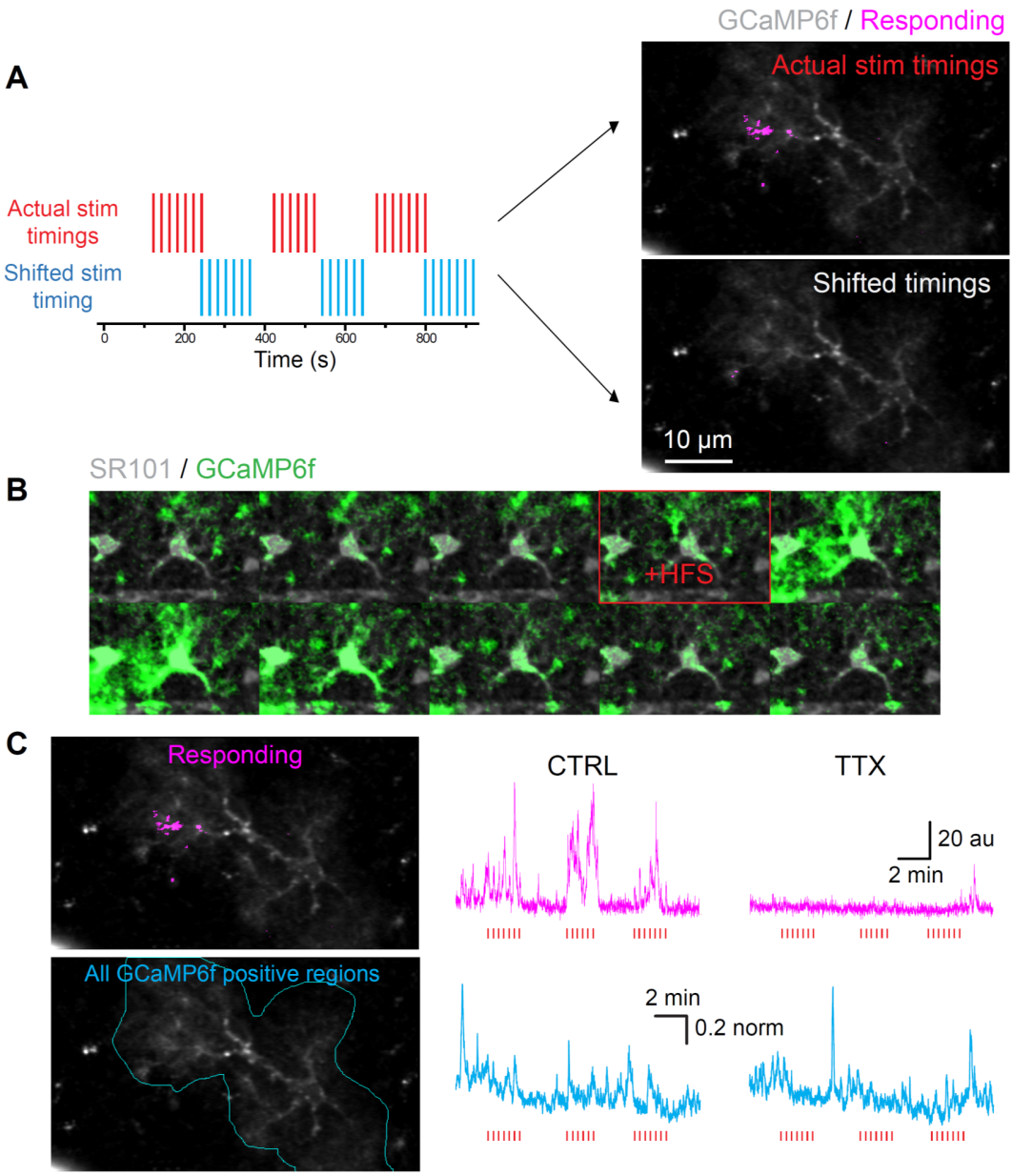


**Fig. S11. Methodological issues in the study of the relationship between axonal firing and astrocytic $Ca^{2+}$ responses.**

**(A)** Validation of our computer-assisted detection of the responding regions within the total imaged volume of an astrocyte in minimal axonal stimulation experiments. Given the very large number of voxels encompassing the total imaged astrocyte volume in "blind" stimulation experiments, a potential problem of our normalized cumulative cross-correlation approach (see Methods) is that it may detect voxels correlated to the electrical stimulation purely by chance (the so-called "Million-monkey" problem). In order to control for such occurrence, we have generated shifted ("scrambled") electrical stimulation traces (*left,* blue protocol) that were fed into the

program together with the real $Ca^{2+}$ imaging data, while keeping the positive correlation threshold and all other parameters intact. In all cases, the "scrambled" traces produced much fewer positively correlated voxels (*right*, bottom image) compared to the real stimulator data (*left,* red protocol; *right*, top image), and such "positive" voxels were randomly scattered throughout the structure. **(B)** The likelihood of positive detection of an astrocytic $Ca^{2+}$ response to axonal firing is increased by the size of such response. The representative time-series of average projection images of the GCaMP6f signal shows the effect of tetanic axonal stimulation (HFS) in inducing a large, "global-like" $Ca^{2+}$ response in the astrocyte spreading over most of its structure and across multiple planes. These types of events are likely to be detected even with conventional 2D imaging approaches. Each frame represents an average over 3 seconds of activity. **(C)** Inappropriate ROI selection may lead to underestimate the effect of TTX on astrocyte $Ca^{2+}$ activity (the "dilution" problem). *Top*: traces show that TTX effectively blocks the $Ca^{2+}$ activity evoked by small axonal stimuli when the ROI is confined to the identified responding parts of the astrocyte. *Bottom*: when the size of the selected ROI is larger, e.g., comprising all the GCaMP6f-positive regions of the astrocyte, the result is that the stimulus-related, TTX-sensitive component is "diluted" in the stimulus-unrelated endogenous activity of the astrocyte, resulting in an apparent full lack of TTX-sensitivity (for further discussion see Text S1).

**Supplemental Text S1. A controversial issue: TTX-sensitivity of basal $Ca^{2+}$ activity in astrocytes**

There is good evidence that $Ca^{2+}$ activity in astrocytes starts at very early developmental stages (P2-P14), even before the establishment of mature neuronal connections and a fully functional circuitry. This early activity was reported by several studies to be TTX-insensitive, suggesting that it is intrinsically generated by the astrocytes, independently of neuronal firing (*43, 56, 57*). By P14 the intrinsic activity appears, however, to be significantly attenuated with respect to P4 (down to 20%, (*56*). On the other hand, in the course of the third postnatal week (P17-P21, (*58*)) and later on (P30-P40, (*14*)) some studies reported the presence of a TTX-sensitive component in the basal astrocytic $Ca^{2+}$ activity. The latter observation was not, however, confirmed by other studies (*26, 40*), leaving the issue of TTX sensitivity uncertain. Observations made in the present study and further methodological considerations suggest that there can be explanations for these apparent contradictory reports.

*The dilution problem*

In this project, we tested the effect of TTX on: (a) basal $Ca^{2+}$ activity in astrocytes from P30-40 hippocampal slices displaying sparse neuronal firing (*14*); (b) upon minimal axonal stimulation. At first glance, results of these two sets of experiments were inconsistent. Thus, while TTX mildly inhibited $Ca^{2+}$ activity in astrocytic processes in basal condition (on average: -43.9 ± 13.4%, Fig 4B), it fully blocked the astrocytic $Ca^{2+}$ response to minimal evoked neuronal activity in responding regions (Fig. 7B). Further analysis showed, however, that the mild effect did not correspond to a weak sensitivity of the basal $Ca^{2+}$ activity to TTX. Instead, it revealed that sensitivity by different processes was different, with about half of them being strongly TTX-sensitive, and the other half only partially sensitive or not sensitive at all. This heterogeneity between different processes, which is likely present also more locally within individual processes, highlights a methodological issue that we can call the "dilution problem". This problem occurs when researches inadvertently associate in their measures TTX-sensitive and TTX-insensitive responses, thereby diluting the real, strong effect of TTX on only one component of the astrocyte $Ca^{2+}$ activity. Depending on how the analysis is performed, the same problem can occur even when studying the $Ca^{2+}$ activity induced in astrocytes by neuronal firing, which by definition has to be, and is, TTX-dependent (Fig. 7B,C). Thus, the astrocyte regions reliably responding to minimal evoked neuronal firing are small in size (about 0.5 % of the astrocyte volume). This makes them difficult to pinpoint in the bulk of the endogenous $Ca^{2+}$ activity of the astrocyte, in the absence of any spatial and/or temporal cue (e.g. the position of the stimulated axon and/or the timing of stimulation). Fig. S11C exemplifies once again the "dilution problem" and shows the critical importance of correctly selecting the ROI containing the TTX-sensitive component. Thus, if the selected ROI does not correspond in size to the real responding region, but is wider, the TTX-sensitive component gets diluted in the TTX-insensitive one, with the dilution being proportional to the mismatch in size. As a result, the TTX effect appears to be smaller than really is (Fig. S11B). If the mismatch is big, it may eventually get fully undetected (Fig. S11C).

*Other factors that may affect detection of a TTX-sensitive component of basal astrocytic $Ca^{2+}$ activity in acute brain slice preparations*

In addition to an intrinsic biological heterogeneity of the astrocytic $Ca^{2+}$ activity, e.g., involving microdomains that are predominantly TTX-sensitive (loci of synaptic contacts, (*15*)) vs TTX-

insensitive (e.g, mitochondrial locations along processes, (*40*)), there can be additional experimental factors that may lead to detect more or less TTX-sensitive $Ca^{2+}$ activity:

1) *Age of the animals and circuitry investigated in acute slice preparations*. As indicated above, the proportion of TTX-sensitive and TTX-insensitive astrocyte activity seems to be influenced by the developmental stage, and therefore by the age of the animals from which acute slice preparations are made. Moreover, the type of circuit investigated is relevant. Certain brain areas are denervated by slice preparation, paradoxically resulting in sPSC frequency being equal to mPSC frequency in TTX. This situation is seen for instance in the cerebellar cortex (*59, 60*) and is likely present also in cortical slices with e.g. transected thalamic afferents. In contrast, in horizontal hippocampal slices, where some connectivity between spontaneously active EC and DG is preserved, we experimentally verified that TTX application reduces sEPSC frequency by 30-50% (*14, 61*), which makes this area a suitable target for studying the TTX effect in astrocytes.
2) *Location of the astrocyte recordings in the slice preparation.* Cells in slices can exhibit a large heterogeneity due to variability in their microenvironment. Again, this can be biological variability, but also "experimental" variability. A predominant factor is the slicing process itself. For instance, some astrocytes (or parts of them) may have more of their axonal inputs transected than others and may therefore be less sensitive to TTX. Logically, astrocytes located closer to the slice surface are likely to be in this situation. Astrocytes on the surface may also experience lower levels of transmitters, factors, or ions ($K^+$) due to washout/interchange with the bath aCSF. On the other hand, astrocytes (or their processes) located deeper in the slice can be surrounded by a more anoxic tissue that may have different functional properties and metabolic requirements compared to more oxygenated layers of the slice.
3) *Properties of the $Ca^{2+}$ indicators.* Another aspect requiring consideration is the suitability of the $Ca^{2+}$ indicators used in assessing the TTX-sensitive component of basal astrocytic $Ca^{2+}$ activity. Indicators with low SNR, including first generation GECIs (GCaMP3), may under-report some of the smaller/faster $Ca^{2+}$ events, among which could be those associated with low-level neuronal activity. This is particularly true of membrane-bound GECI, which will also tend to over-buffer small events due to very high concentration at the plasma membrane in small compartments.

**Supplemental Movie Captions: S1-S4**

**Movie S1**
Comparative morphology of an astrocyte in 3D vs 2D.

**Movie S2**
Comparison of $Ca^{2+}$ activity observable in 3D vs 2D.

**Movie S3**
$Ca^{2+}$ imaging of astrocytes in vivo in awake mouse.

**Movie S4**
Axon-astrocyte morphological interactions in 3D vs 2D.

**References**


1. K. E. Poskanzer, R. Yuste, Astrocytes regulate cortical state switching in vivo. *Proc. Natl. Acad. Sci. U.S.A.* **113**, E2675–E2684 (2016). doi:10.1073/pnas.1520759113 Medline

2. A. Volterra, N. Liaudet, I. Savtchouk, Astrocyte $Ca^{2+}$ signalling: An unexpected complexity. *Nat. Rev. Neurosci.* **15**, 327–335 (2014). doi:10.1038/nrn3725 Medline

3. A. Araque, G. Carmignoto, P. G. Haydon, S. H. R. Oliet, R. Robitaille, A. Volterra, Gliotransmitters travel in time and space. *Neuron* **81**, 728–739 (2014). doi:10.1016/j.neuron.2014.02.007 Medline

4. G. Perea, M. Navarrete, A. Araque, Tripartite synapses: Astrocytes process and control synaptic information. *Trends Neurosci.* **32**, 421–431 (2009). doi:10.1016/j.tins.2009.05.001 Medline

5. N. Bazargani, D. Attwell, Astrocyte calcium signaling: The third wave. *Nat. Neurosci.* **19**, 182–189 (2016). doi:10.1038/nn.4201 Medline

6. B. A. MacVicar, E. A. Newman, Astrocyte regulation of blood flow in the brain. *Cold Spring Harb. Perspect. Biol.* **7**, a020388 (2015). doi:10.1101/cshperspect.a020388 Medline

7. J. Schummers, H. Yu, M. Sur, Tuned responses of astrocytes and their influence on hemodynamic signals in the visual cortex. *Science* **320**, 1638–1643 (2008). doi:10.1126/science.1156120 Medline

8. A. Nimmerjahn, E. A. Mukamel, M. J. Schnitzer, Motor behavior activates Bergmann glial networks. *Neuron* **62**, 400–412 (2009). doi:10.1016/j.neuron.2009.03.019 Medline

9. K. Kanemaru, H. Sekiya, M. Xu, K. Satoh, N. Kitajima, K. Yoshida, Y. Okubo, T. Sasaki, S. Moritoh, H. Hasuwa, M. Mimura, K. Horikawa, K. Matsui, T. Nagai, M. Iino, K. F. Tanaka, In vivo visualization of subtle, transient, and local activity of astrocytes using an ultrasensitive $Ca^{2+}$ indicator. *Cell Rep.* **8**, 311–318 (2014). doi:10.1016/j.celrep.2014.05.056 Medline

10. X. Wang, N. Lou, Q. Xu, G.-F. Tian, W. G. Peng, X. Han, J. Kang, T. Takano, M. Nedergaard, Astrocytic $Ca^{2+}$ signaling evoked by sensory stimulation in vivo. *Nat. Neurosci.* **9**, 816–823 (2006). doi:10.1038/nn1703 Medline

11. M. Navarrete, G. Perea, D. Fernandez de Sevilla, M. Gómez-Gonzalo, A. Núñez, E. D. Martín, A. Araque, Astrocytes mediate in vivo cholinergic-induced synaptic plasticity. *PLOS Biol.* **10**, e1001259 (2012). doi:10.1371/journal.pbio.1001259 Medline

12. C. Henneberger, T. Papouin, S. H. Oliet, D. A. Rusakov, Long-term potentiation depends on release of D-serine from astrocytes. *Nature* **463**, 232–236 (2010). doi:10.1038/nature08673 Medline

13. R. Min, T. Nevian, Astrocyte signaling controls spike timing-dependent depression at neocortical synapses. *Nat. Neurosci.* **15**, 746–753 (2012). doi:10.1038/nn.3075 Medline

14. M. A. Di Castro, J. Chuquet, N. Liaudet, K. Bhaukaurally, M. Santello, D. Bouvier, P. Tiret, A. Volterra, Local $Ca^{2+}$ detection and modulation of synaptic release by astrocytes. *Nat. Neurosci.* **14**, 1276–1284 (2011). doi:10.1038/nn.2929 Medline

15. A. Panatier, J. Vallée, M. Haber, K. K. Murai, J.-C. Lacaille, R. Robitaille, Astrocytes are endogenous regulators of basal transmission at central synapses. *Cell* **146**, 785–798 (2011). doi:10.1016/j.cell.2011.07.022 Medline

16. G. R. Gordon, H. B. Choi, R. L. Rungta, G. C. Ellis-Davies, B. A. MacVicar, Brain metabolism dictates the polarity of astrocyte control over arterioles. *Nature* **456**, 745–749 (2008). doi:10.1038/nature07525 Medline

17. I. R. Winship, N. Plaa, T. H. Murphy, Rapid astrocyte calcium signals correlate with neuronal activity and onset of the hemodynamic response in vivo. *J. Neurosci.* **27**, 6268–6272 (2007). doi:10.1523/JNEUROSCI.4801-06.2007 Medline

18. H. L. Xu, L. Mao, S. Ye, C. Paisansathan, F. Vetri, D. A. Pelligrino, Astrocytes are a key conduit for upstream signaling of vasodilation during cerebral cortical neuronal activation in vivo. *Am. J. Physiol. Heart Circ. Physiol.* **294**, H622–H632 (2008). doi:10.1152/ajpheart.00530.2007 Medline

19. M. R. Metea, E. A. Newman, Glial cells dilate and constrict blood vessels: A mechanism of neurovascular coupling. *J. Neurosci.* **26**, 2862–2870 (2006). doi:10.1523/JNEUROSCI.4048-05.2006 Medline

20. B. L. Lind, A. R. Brazhe, S. B. Jessen, F. C. Tan, M. J. Lauritzen, Rapid stimulus-evoked astrocyte $Ca^{2+}$ elevations and hemodynamic responses in mouse somatosensory cortex in vivo. *Proc. Natl. Acad. Sci. U.S.A.* **110**, E4678–E4687 (2013). doi:10.1073/pnas.1310065110 Medline

21. Y. Otsu, K. Couchman, D. G. Lyons, M. Collot, A. Agarwal, J.-M. Mallet, F. W. Pfrieger, D. E. Bergles, S. Charpak, Calcium dynamics in astrocyte processes during neurovascular coupling. *Nat. Neurosci.* **18**, 210–218 (2015). doi:10.1038/nn.3906 Medline

22. C. Agulhon, T. A. Fiacco, K. D. McCarthy, Hippocampal short- and long-term plasticity are not modulated by astrocyte $Ca^{2+}$ signaling. *Science* **327**, 1250–1254 (2010). doi:10.1126/science.1184821 Medline

23. W. Sun, E. McConnell, J.-F. Pare, Q. Xu, M. Chen, W. Peng, D. Lovatt, X. Han, Y. Smith, M. Nedergaard, Glutamate-dependent neuroglial calcium signaling differs between young and adult brain. *Science* **339**, 197–200 (2013). doi:10.1126/science.1226740 Medline

24. K. Nizar, H. Uhlirova, P. Tian, P. A. Saisan, Q. Cheng, L. Reznichenko, K. L. Weldy, T. C. Steed, V. B. Sridhar, C. L. MacDonald, J. Cui, S. L. Gratiy, S. Sakadzić, D. A. Boas, T. I.

Beka, G. T. Einevoll, J. Chen, E. Masliah, A. M. Dale, G. A. Silva, A. Devor, In vivo stimulus-induced vasodilation occurs without IP3 receptor activation and may precede astrocytic calcium increase. *J. Neurosci.* **33**, 8411–8422 (2013). doi:10.1523/JNEUROSCI.3285-12.2013 Medline

25. D. E. Bonder, K. D. McCarthy, Astrocytic Gq-GPCR-linked IP3R-dependent $Ca^{2+}$ signaling does not mediate neurovascular coupling in mouse visual cortex in vivo. *J. Neurosci.* **34**, 13139–13150 (2014). doi:10.1523/JNEUROSCI.2591-14.2014 Medline

26. M. D. Haustein, S. Kracun, X.-H. Lu, T. Shih, O. Jackson-Weaver, X. Tong, J. Xu, X. W. Yang, T. J. O'Dell, J. S. Marvin, M. H. Ellisman, E. A. Bushong, L. L. Looger, B. S. Khakh, Conditions and constraints for astrocyte calcium signaling in the hippocampal mossy fiber pathway. *Neuron* **82**, 413–429 (2014). doi:10.1016/j.neuron.2014.02.041 Medline

27. W. Göbel, B. M. Kampa, F. Helmchen, Imaging cellular network dynamics in three dimensions using fast 3D laser scanning. *Nat. Methods* **4**, 73–79 (2007). doi:10.1038/nmeth989 Medline

28. T. W. Chen, T. J. Wardill, Y. Sun, S. R. Pulver, S. L. Renninger, A. Baohan, E. R. Schreiter, R. A. Kerr, M. B. Orger, V. Jayaraman, L. L. Looger, K. Svoboda, D. S. Kim, Ultrasensitive fluorescent proteins for imaging neuronal activity. *Nature* **499**, 295–300 (2013). doi:10.1038/nature12354 Medline

29. H. Dana, B. Mohar, Y. Sun, S. Narayan, A. Gordus, J. P. Hasseman, G. Tsegaye, G. T. Holt, A. Hu, D. Walpita, R. Patel, J. J. Macklin, C. I. Bargmann, M. B. Ahrens, E. R. Schreiter, V. Jayaraman, L. L. Looger, K. Svoboda, D. S. Kim, Sensitive red protein calcium indicators for imaging neural activity. *eLife* **5**, e12727 (2016). doi:10.7554/eLife.12727 Medline

30. See supplementary materials.

31. R. Srinivasan, B. S. Huang, S. Venugopal, A. D. Johnston, H. Chai, H. Zeng, P. Golshani, B. S. Khakh, $Ca^{2+}$ signaling in astrocytes from $Ip3r2^{-/-}$ mice in brain slices and during startle responses in vivo. *Nat. Neurosci.* **18**, 708–717 (2015). doi:10.1038/nn.4001 Medline

32. K. J. Sekiguchi, P. Shekhtmeyster, K. Merten, A. Arena, D. Cook, E. Hoffman, A. Ngo, A. Nimmerjahn, Imaging large-scale cellular activity in spinal cord of freely behaving mice. *Nat. Commun.* **7**, 11450 (2016). doi:10.1038/ncomms11450 Medline

33. P. O. Polack, J. Friedman, P. Golshani, Cellular mechanisms of brain state-dependent gain modulation in visual cortex. *Nat. Neurosci.* **16**, 1331–1339 (2013). doi:10.1038/nn.3464 Medline

34. M. Avoli, M. Barbarosie, A. Lücke, T. Nagao, V. Lopantsev, R. Köhling, Synchronous GABA-mediated potentials and epileptiform discharges in the rat limbic system in vitro. *J. Neurosci.* **16**, 3912–3924 (1996). Medline

35. M. P. Witter, The perforant path: Projections from the entorhinal cortex to the dentate gyrus. *Prog. Brain Res.* **163**, 43–61 (2007). doi:10.1016/S0079-6123(07)63003-9 Medline

36. N. V. Povysheva, G. Gonzalez-Burgos, A. V. Zaitsev, S. Kröner, G. Barrionuevo, D. A. Lewis, L. S. Krimer, Properties of excitatory synaptic responses in fast-spiking interneurons and pyramidal cells from monkey and rat prefrontal cortex. *Cereb. Cortex* **16**, 541–552 (2006). doi:10.1093/cercor/bhj002 Medline

37. M. Paukert, A. Agarwal, J. Cha, V. A. Doze, J. U. Kang, D. E. Bergles, Norepinephrine controls astroglial responsiveness to local circuit activity. *Neuron* **82**, 1263–1270 (2014). doi:10.1016/j.neuron.2014.04.038 Medline

38. K. Zheng, L. Bard, J. P. Reynolds, C. King, T. P. Jensen, A. V. Gourine, D. A. Rusakov, Time-resolved imaging reveals heterogeneous landscapes of nanomolar $Ca^{2+}$ in neurons and astroglia. *Neuron* **88**, 277–288 (2015). doi:10.1016/j.neuron.2015.09.043 Medline

39. J. G. Jackson, M. B. Robinson, Reciprocal regulation of mitochondrial dynamics and calcium signaling in astrocyte processes. *J. Neurosci.* **35**, 15199–15213 (2015). doi:10.1523/JNEUROSCI.2049-15.2015 Medline

40. A. Agarwal, P.-H. Wu, E. G. Hughes, M. Fukaya, M. A. Tischfield, A. J. Langseth, D. Wirtz, D. E. Bergles, Transient opening of the mitochondrial permeability transition pore induces microdomain calcium transients in astrocyte processes. *Neuron* **93**, 587–605.e7 (2017). doi:10.1016/j.neuron.2016.12.034

41. K. J. Kim, J. A. Iddings, J. E. Stern, V. M. Blanco, D. Croom, S. A. Kirov, J. A. Filosa, Astrocyte contributions to flow/pressure-evoked parenchymal arteriole vasoconstriction. *J. Neurosci.* **35**, 8245–8257 (2015). doi:10.1523/JNEUROSCI.4486-14.2015 Medline

42. K. Schulz, E. Sydekum, R. Krueppel, C. J. Engelbrecht, F. Schlegel, A. Schröter, M. Rudin, F. Helmchen, Simultaneous BOLD fMRI and fiber-optic calcium recording in rat neocortex. *Nat. Methods* **9**, 597–602 (2012). doi:10.1038/nmeth.2013 Medline

43. W. J. Nett, S. H. Oloff, K. D. McCarthy, Hippocampal astrocytes in situ exhibit calcium oscillations that occur independent of neuronal activity. *J. Neurophysiol.* **87**, 528–537 (2002). Medline

44. P. G. Hirrlinger, A. Scheller, C. Braun, J. Hirrlinger, F. Kirchhoff, Temporal control of gene recombination in astrocytes by transgenic expression of the tamoxifen-inducible DNA recombinase variant CreERT2. *Glia* **54**, 11–20 (2006). doi:10.1002/glia.20342 Medline

45. C. Nolte, M. Matyash, T. Pivneva, C. G. Schipke, C. Ohlemeyer, U.-K. Hanisch, F. Kirchhoff, H. Kettenmann, GFAP promoter-controlled EGFP-expressing transgenic mice: A tool to visualize astrocytes and astrogliosis in living brain tissue. *Glia* **33**, 72–86 (2001). doi:10.1002/1098-1136(20010101)33:1<72:AID-GLIA1007>3.0.CO;2-A Medline

46. S. Habbas, M. Santello, D. Becker, H. Stubbe, G. Zappia, N. Liaudet, F. R. Klaus, G. Kollias, A. Fontana, C. R. Pryce, T. Suter, A. Volterra, Neuroinflammatory TNFα impairs memory via astrocyte signaling. *Cell* **163**, 1730–1741 (2015). doi:10.1016/j.cell.2015.11.023 Medline

47. J. Ding, A. F. Luo, L. Hu, D. Wang, F. Shao, Structural basis of the ultrasensitive calcium indicator GCaMP6. *Sci. China Life Sci.* **57**, 269–274 (2014). doi:10.1007/s11427-013-4599-5 Medline

48. A. Nimmerjahn, F. Kirchhoff, J. N. Kerr, F. Helmchen, Sulforhodamine 101 as a specific marker of astroglia in the neocortex in vivo. *Nat. Methods* **1**, 31–37 (2004). doi:10.1038/nmeth706 Medline

49. C. Schnell, Y. Hagos, S. Hülsmann, Active sulforhodamine 101 uptake into hippocampal astrocytes. *PLOS ONE* **7**, e49398 (2012). doi:10.1371/journal.pone.0049398 Medline

50. A. Holtmaat, T. Bonhoeffer, D. K. Chow, J. Chuckowree, V. De Paola, S. B. Hofer, M. Hübener, T. Keck, G. Knott, W.-C. A. Lee, R. Mostany, T. D. Mrsic-Flogel, E. Nedivi, C. Portera-Cailliau, K. Svoboda, J. T. Trachtenberg, L. Wilbrecht, Long-term, high-resolution imaging in the mouse neocortex through a chronic cranial window. *Nat. Protoc.* **4**, 1128–1144 (2009). doi:10.1038/nprot.2009.89 Medline

51. K. Masamoto, Y. Tomita, H. Toriumi, I. Aoki, M. Unekawa, H. Takuwa, Y. Itoh, N. Suzuki, I. Kanno, Repeated longitudinal in vivo imaging of neuro-glio-vascular unit at the peripheral boundary of ischemia in mouse cerebral cortex. *Neuroscience* **212**, 190–200 (2012). doi:10.1016/j.neuroscience.2012.03.034 Medline

52. N. Medvedev, V. Popov, C. Henneberger, I. Kraev, D. A. Rusakov, M. G. Stewart, Glia selectively approach synapses on thin dendritic spines. *Philos. Trans. R. Soc. London Ser. B* **369**, 20140047 (2014). doi:10.1098/rstb.2014.0047 Medline

53. B. K. Andrásfalvy, G. L. Galiñanes, D. Huber, M. Barbic, J. J. Macklin, K. Susumu, J. B. Delehanty, A. L. Huston, J. K. Makara, I. L. Medintz, Quantum dot-based multiphoton fluorescent pipettes for targeted neuronal electrophysiology. *Nat. Methods* **11**, 1237–1241 (2014). doi:10.1038/nmeth.3146 Medline

54. M. Raastad, Extracellular activation of unitary excitatory synapses between hippocampal CA3 and CA1 pyramidal cells. *Eur. J. Neurosci.* **7**, 1882–1888 (1995). doi:10.1111/j.1460-9568.1995.tb00709.x Medline

55. E. Meijering, M. Jacob, J.-C. F. Sarria, P. Steiner, H. Hirling, M. Unser, Design and validation of a tool for neurite tracing and analysis in fluorescence microscopy images. *Cytometry A* **58**, 167–176 (2004). doi:10.1002/cyto.a.20022 Medline

56. H. R. Parri, T. M. Gould, V. Crunelli, Spontaneous astrocytic $Ca^{2+}$ oscillations in situ drive NMDAR-mediated neuronal excitation. *Nat. Neurosci.* **4**, 803–812 (2001). doi:10.1038/90507 Medline

57. F. Aguado, J. F. Espinosa-Parrilla, M. A. Carmona, E. Soriano, Neuronal activity regulates correlated network properties of spontaneous calcium transients in astrocytes in situ. *J. Neurosci.* **22**, 9430–9444 (2002). Medline

58. E. Barat, S. Boisseau, C. Bouyssières, F. Appaix, M. Savasta, M. Albrieux, Subthalamic nucleus electrical stimulation modulates calcium activity of nigral astrocytes. *PLOS ONE* **7**, e41793 (2012). doi:10.1371/journal.pone.0041793 Medline

59. I. Savtchouk, S. J. Liu, Remodeling of synaptic AMPA receptor subtype alters the probability and pattern of action potential firing. *J. Neurosci.* **31**, 501–511 (2011). doi:10.1523/JNEUROSCI.2608-10.2011 Medline

60. I. Savtchouk, L. Sun, C. L. Bender, Q. Yang, G. Szabó, S. Gasparini, S. J. Liu, Topological regulation of synaptic AMPA receptor expression by the RNA-binding protein CPEB3. *Cell Rep.* **17**, 86–103 (2016). doi:10.1016/j.celrep.2016.08.094 Medline

61. P. Jourdain, L. H. Bergersen, K. Bhaukaurally, P. Bezzi, M. Santello, M. Domercq, C. Matute, F. Tonello, V. Gundersen, A. Volterra, Glutamate exocytosis from astrocytes controls synaptic strength. *Nat. Neurosci.* **10**, 331–339 (2007). doi:10.1038/nn1849 Medline